Hydrogenation of CO2 to Methanol by Pt Nanoparticles Encapsulated in UiO-67: Deciphering the Role of the Metal-Organic Framework

Original Citation:

Availability:

This version is available http://hdl.handle.net/2318/1739981 since 2025-01-20T15:06:36Z

Published version:

DOI:10.1021/jacs.9b10873

Hydrogenation of CO_2 to Methanol by Pt Nanoparticles Encapsulated in UiO-67: Deciphering the Role of the MOF

Emil S. Gutterød[a], Andrea Lazzarini[a], Torstein Fjermestad[b], Gurpreet Kaur[a], Maela Manzoli[c], Silvia Bordiga[a,d], Stian Svelle[a], Karl P. Lillerud[a], Egill Skúlason[e], Sigurd Øien-Ødegaard[a], Ainara Nova[b], Unni Olsbye[a]*

[a]Centre for Materials Science and Nanotechnology, Department of Chemistry, University of Oslo, Sem Saelandsvei 26, N-0315 Oslo, Norway

[b]Hylleraas Centre for Quantum Molecular Sciences, Department of Chemistry, University of Oslo, P.O. Box 1033, Blindern, N-0315 Oslo, Norway

[c]Department of Drug Science and Technology and NIS - Centre for Nanostructured Interfaces and Surfaces, University of Turin, Via P. Giuria 9, Turin 10125, Italy

[d]Department of Chemistry, NIS Interdepartmental Centre and INSRM reference centre, University of Turin, via Quarello 15A, I-10135 Turin, Italy

[e]Science Institute and Faculty of Industrial Engineering, Mechanical Engineering and Computer Science, University of Iceland, VR-III, 107 Reykjavik, Iceland

Abstract

Metal-organic frameworks (MOFs) show great prospect as catalysts and catalyst support materials. Yet, studies that address their dynamic, kinetic and mechanistic role in target reactions are scarce. In this study, an exceptionally stable MOF catalyst consisting of Pt nanoparticles (NPs) embedded in a Zr-based UiO-67 MOF was subject to steady-state and transient kinetic studies involving H/D and ^{13}C /^{12}C exchange, coupled with operando infrared spectroscopy and density functional theory (DFT) modeling, targeting methanol formation from CO_2/H_2 feeds at 170 °C and 1-8 bar pressure. The study revealed that methanol is formed at the interface between the Pt NPs and defect Zr nodes, via formate species attached to the Zr nodes. Methanol formation is mechanistically separated from the formation of co-products CO and methane, except for hydrogen activation on the Pt NPs. Careful analysis of transient data revealed that the number of formate intermediates was higher than the number of open Zr sites in the MOF lattice around each Pt NP. Hence, additional Zr sites must be available to formate formation. DFT modelling revealed that Pt NP growth is sufficiently energetically favored to enable displacement of linkers and creation of open Zr sites during pretreatment. However, linker displacement during formate formation is energetically disfavored, in line with the excellent catalyst stability observed experimentally. Overall, the study provides firm

evidence that methanol is formed at the interface of Pt NPs and linker-deficient Zr_6O_8 nodes resting on the Pt NP surface.

Keywords: CO_2 hydrogenation, methanol, formate, transient kinetic analysis, kinetic isotope effect, operando FTIR, DFT, MOF, UiO-67.

Introduction

Atmospheric levels of CO_2 have risen at an alarming rate since the first half of the 20th century following our continuous and increasing use of fossil fuels. Large cuts in CO_2 emissions can be made through utilization of greener alternatives of energy production such as solar and wind power; however, these energy sources suffer from lack of continuity in energy output and requires efficient methods for large scale energy storage in order to compete with fossil fuels.[1] One of the solutions to this problem is production of easily stored liquid fuels with high volumetric and gravimetric energy density, such as methanol, from CO_2 and green hydrogen.[2] This allows for continued use of already existing infrastructure.[3] Substantial research efforts have already been dedicated to the topic of valorizing CO_2 through hydrogenation, mainly with focus on the reverse water-gas shift (RWGS) reaction, methanation and methanol production.[4-13]

The product distribution of CO_2 hydrogenation varies significantly with the nature of the catalyst and operating conditions.[7] Most prior studies show that Pt-based systems are highly selective for the RWGS reaction, with minor selectivity towards methane.[11, 14-19] In that respect, Kattel et al.[18] performed a computational study of CO_2 hydrogenation over Pt nanoparticles supported on SiO_2 and TiO_2. They concluded that a RWGS and CO hydrogenation path, forming CO and small amounts of methane, dominate over those materials. This finding is in agreement with experimental evidence of CO formation mainly via surface carbonates.[15, 16]

Surface formates are also observed in several studies of the RWGS[15, 16, 20, 21] and of WGS[22-24] reactions; however, the significance of such a pathway over Pt-based catalysts is debated. In this regard, Burch, Goguet and Meunier[23] conducted a critical analysis of the experimental evidence for and against a formate mechanism over highly active Pt and Au WGS catalysts. They argue that most published results do not provide definite evidence for or against a formate pathway for the WGS reaction, and in the cases where reliable data are available, it is at most a minor and slow reaction pathway.

Recent studies show that when supporting Pt on a methane producing Co-oxide catalyst, methanol selectivity is observable under favorable conditions of low temperature and elevated pressure[25-27]. Furthermore, one prior study[28] demonstrated selectivity towards methanol over oxide-supported Pt where the supports alone are inactive in CO_2 hydrogenation: out of a set of catalysts producing mainly CO (> 91 %), Pt/ZrO_2 showed the highest CH_3OH selectivity, reaching 6 % at 200 °C and 10 atm pressure.

Over the Zr-MOFs UiO-66 and -67, functionalized with Cu and Cu/Zn, high methanol selectivity is ascribed to an important role of the Zr-MOF interface in the reaction. Rungtaweevoranit et al.[29] found XPS evidence of Zr reduction in the presence of Cu when studying Cu NPs deposited on UiO-66 as a model system for the encapsulated version of the catalyst (i.e. Cu in UiO-66). Similar findings from XPS on CuZn@UiO-67 samples with 100% bipyridine-type linkers treated with reaction gas showed indications of Zr(IV) reduction to Zr(III), argued as caused by H adsorption.[30] In combination with H_2- and CO_2-TPD results, the authors suggested participation of the Zr-cluster in the reaction by means of H-spillover from Cu and CO_2 adsorption on unsaturated Zr-sites. When the catalyst was prepared with regular UiO-67 (i.e. biphenyl-type linkers), both the CH_3OH selectivity and catalytic stability decreased. Although the CuZn@UiO-67 material showed substantial activity in methanol formation, notably, both the crystallinity and specific surface area of the MOF were severely reduced already by the deposition of copper. Thus, the material did not exhibit the well-defined MOF structure of UiO-67 during the subsequent experiments.[30]

In a previous contribution, we reported the CO_2 hydrogenation activity and selectivity of an exceptionally stable Pt Zr-MOF catalyst, UiO-67-Pt, at ambient pressure. This catalyst maintains its well-defined MOF structure even after long-term operation and is therefore well suited as a model system for studying the influence of the MOF framework on the reaction. In the current study, the focus is set on elucidating the role of the UiO-67 framework in CO_2 hydrogenation to methanol through a kinetic investigation. In addition to standard steady-state kinetic measurements, we employ H/D- and $^{13}C/^{12}C$ SSITKA, and *operando* FT-IR measurements, methods scarcely employed in MOF catalysis literature. In combination with DFT calculations, this work reveals unprecedented insight in the Pt–Zr-MOF interplay that leads to methanol formation during conversion of CO_2/H_2 mixtures at 170 °C and 1–8 bar.

Experimental Details

Details of material preparation and standard characterization methods (N_2 adsorption, ^1H-NMR, EDX, TGA, TEM and CO-chemisorption) are provided in the SI.

Operando FT-IR spectroscopy was performed using a Bruker Vertex70 instrument equipped with a liquid nitrogen-cooled MCT detector. Each spectrum was collected by averaging 64 acquisitions with a resolution of 2 cm^{-1}. The sample (pressed in a self-sustained pellet of approx. 4 mg) was mounted inside a low free-volume cell from AABSPEC (model #CXX), by which pressure, temperature and gas flow are controllable. Due to the low sample amount, the CO_2 conversion was too low to be determined reliably and parallel experiments under comparable conditions were performed with the focus on gas-phase analysis (vide infra). The sample was activated at 350 °C (5 °C/min ramp) in 10 % H_2/He (10 ml/min) for 4 hours, and then cooled to 170 °C in 10 ml/min He. The sample was kept under CO_2 hydrogenation ($CO_2/H_2 = 1/6$, 10 ml/min) reaction conditions for two hours, before the H_2 flow was exchanged to D_2.

Catalytic testing was performed in a fixed-bed flow setup with a straight stainless steel reactor (7 mm I.D.) operated under 1–8 bar, where effluent species is analyzed with an on-line Q-MS (Pfeiffer) and GC-TCD-FID (Agilent). The MOF samples were reduced for 4 hours at 350°C (5 °C/min ramp) in 20 ml/(min·0.1g_{cat}) flow of 10 % H_2/Ar under ambient pressure. Following the activation procedure, the reactor was cooled to 240 °C in inert flow, then operated for 4 hours reaching steady-state under a set of reference conditions (1/6/3 CO_2/H_2/inert, 20 ml/min, 200 mg, $\tau = 0.01$ g_{cat}·min/ml and ambient pressure) before changing conditions. The pre-reduced commercial samples Pt/SiO_2 (abcr), Pt/Al_2O_3 (Chimet) and Pt/C (Chimet), were heated directly to 240 °C under reference conditions, which were maintained until steady state was reached. Dependent on the experimental aim, 0.05–0.2 g catalyst was tested for CO_2 hydrogenation in range: 5–25 % CO_2, 40–90 % H_2, T = 170 °C, p = 1–8 bar and contact time $\tau = 0.004–0.04$ g_{cat}·min/ml. A given set of operating conditions was fixed until steady state was reached and for at least two hours. During kinetic studies, changes in reaction conditions were performed in a random sequence. Each 3–4 set of conditions were the reference conditions. They showed that the change in catalyst performance was negligible during the kinetic studies. As reported in ref.[17] a minor increase in the catalytic activity and change in selectivity is observed for UiO-67-Pt during long-term operation. The same procedure as described above was followed in the H/D exchange experiments but with D_2 instead of H_2. H/D SSITKA experiments were performed by operating the catalysts at steady state under reference conditions, then switching the feed (1/6/3 CO_2/H_2/inert) rapidly to another feed containing D_2 instead of H_2 (1/6/3 CO_2/D_2/inert) using an electronically controlled 4-port 2-way valve. Switches back and forth between the two feeds were performed in intervals of 8 hours. $^{13}CO_2/^{12}CO_2$ SSTIKA experiments were performed in the same manner. The m/z values traced for each specie in the respective experiments are tabulated in Table S1.

Intermediates and catalyst structures were optimized using Density functional theory (DFT) calculations. The calculations were carried out using the mixed Gaussian and plane wave method[31-33] as implemented in CP2K 6.1.[34, 35] The functional was PBE+D3, the atom-centered basis set was DZVP-MOLOPT-SR-GTH,[36] and the plane wave kinetic energy cut-off was 360 Ry. Further details are provided in the SI.

Results and Discussion

The UiO-66 series of Zr-MOFs (UiO-66, -67, -68) consists of Zr_6O_8 nodes connected by dicarboxylate-terminated linkers. The ideal linker-to-node ratio is 6:1, but prior investigations showed that factors like synthesis conditions (type of modulator and concentration, temperature and crystallization time) and activation conditions may strongly affect this ratio, leading to materials that are commonly referred to as having "missing cluster" or "missing linker" defects, respectively[37-43]. Missing linker defects may be capped by modulator, anions of the MOF precursor salts, solvent or OH^-/H_2O pairs.[39, 42, 44, 45]

The current study was carried out using UiO-67 with 90 % biphenyl-4,4'-dicarboxylic acid (BPDC) linkers and 10 % 2,2'-bipyridine-5,5'-dicarboxylic acid (BPYDC) linkers, hereafter called **UiO-67-Pt**. Prior studies have demonstrated that the bipyridine entity in BPYDC is the preferred anchoring site for Pt salts in this MOF.[17, 46-48] In the current study, ^1H NMR analysis of digested material showed that the as-synthesized MOF contained 11 BPYDC linkers, 13 benzoic acid and 2 formic acid ligands, respectively, per 100 BPDC linkers (Table S3). Furthermore, Thermo-Gravimetric Analysis (TGA) measurements indicated that the as-synthesized MOF had a linker-to-node ratio of 5, suggesting that, in addition to benzoic acid and formic acid, the material contained Cl^- or OH^-/H_2O pairs, adding up to an average of 4 out of 24 Zr coordination sites per Zr-node that were not connected to a linker molecule (Table S3).

After wet impregnation with the Pt NP precursor, K_2PtCl_4, the BPYDC and benzoic acid contents of UiO-67-Pt decreased slightly, while the formic acid content increased to 4 per 100 BPDC linkers (Table S2). Activation in a reducing atmosphere (10 % H_2/Ar flow at 350 °C, 1 bar, 4 h) transformed the Pt precursor salt into the active catalytic entity for CO_2 hydrogenation, Pt NPs.[17, 46, 48] In the current case, Transmission Electron Microscopy (TEM) investigations after activation showed the presence of Pt NPs homogeneously dispersed within the MOF framework (Figure S5). The Pt NPs supported on UiO-67 have average diameter of 3.6 ± 0.7 nm (Figure S5), i.e. larger than the diameter of the tetrahedral (1.2 nm) and octahedral (2.3 nm) cavities of the UiO-67 structure. Most of the Pt NPs displayed spherical shape, however, careful inspection revealed the presence of NPs with squared borders and irregular shape, possibly exposing well defined terraces, after activation and after reaction (Figure S5 and Figure S6). Such features can arise from strong Pt-support interaction, and indeed, limited broadening of the Pt NP size distribution was observed after prolonged testing (Figure S6). A schematic illustration of a 3.6 nm Pt particle embedded in an 8 unit cell-enclosed octahedral cavity, mimicking a representative Pt NP observed by TEM, is presented in Scheme 1.

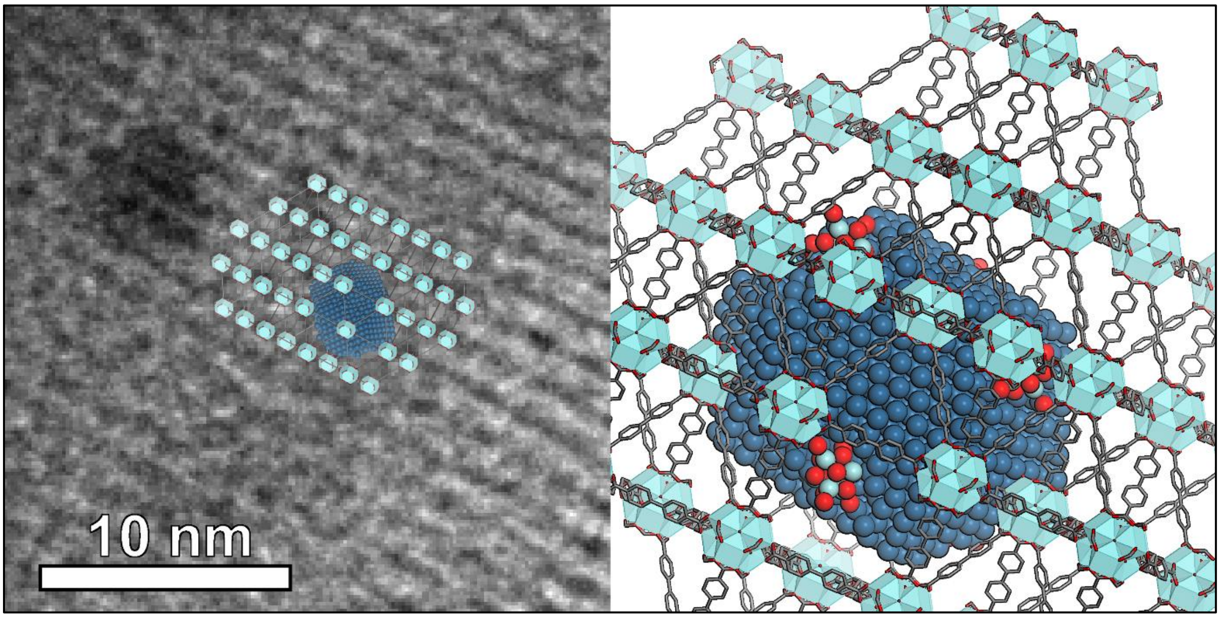

Scheme 1. Left: TEM micrograph showing the close packed (1 1 1) layers of Zr_6 clusters in UiO-67, with a spacing of 15.5 Å, overlaid with a 1600 atom Pt NP in the structure of UiO-67 viewed along (1 1 2) which is perpendicular to (1 1 1). Right: A 1600 atom Pt NP in UiO-67 viewed in the same direction. 6 Zr_6 clusters have been removed to accommodate the NP, and are decorating the NP surface.

CO_2/H_2 conversion and product selectivity obtained over Pt/C, Pt/SiO_2, Pt/Al_2O_3 and UiO-67-Pt at 170 °C and 1–8 bar is shown in Figure 1. Substantial selectivity differences were observed at similar conversion levels (0.4–1.5 %): Over UiO-67-Pt, the methanol selectivity increased from around 3 to 19 %—corresponding to a turn-over-frequency (TOF) of 0.01 s^{-1}—when the pressure increased from 1 to 8 bar (Figure 1). This is, to the best of our knowledge, the second report of significant methanol formation from CO_2 over a Pt-based catalyst where the support alone is inactive in the reaction.[28] Under the same conditions, there was only a slight increase in methane selectivity from 1.2 to 1.6 %. Over Pt/Al_2O_3, both the methane and methanol selectivity reached 10 % under 8 bar pressure (Figure 1). In contrast to UiO-67-Pt, methane selectivity increased substantially with increasing pressure. Finally, over Pt/SiO_2 and Pt/C (Figure 1), CO was the only carbon-containing product observed, in accordance with the theory predictions of Kattel et al. for unsupported Pt NPs.[18] The formation of methanol over UiO-67-Pt points to strong metal-support interactions, as previously reported for Cu NPs embedded in UiO Zr-MOFs,[29, 30] and may suggest that the MOF support plays an active role during reaction, similarly to Al_2O_3 in the Water Gas Shift (WGS) and CO_2 hydrogenation reactions.[8, 24, 49]

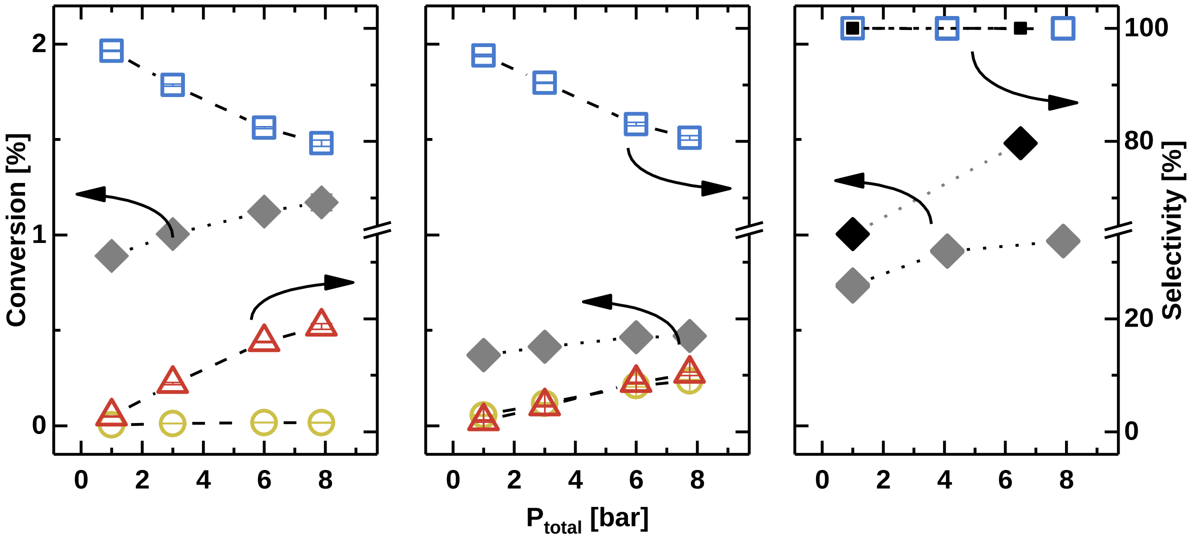

Figure 1. CO_2 conversion (left axes, diamonds) and product selectivity (right axes) during CO_2 hydrogenation under 1–8 bar total reaction pressure and T = 170 °C. Left: UiO-67-Pt. Middle: Pt/Al_2O_3. Right: Pt/SiO_2 (grey, blue) and Pt/C (black). CO, CH_4 and CH_3OH selectivity is depicted as squares, circles and triangles, respectively. $\tau = 0.01\ g_{cat}\cdot min/ml$, $CO_2/H_2/inert = 1/6/3$. For Pt/Al_2O_3 $\tau = 0.02\ g_{cat}\cdot min/ml$.

To further assess the role of Pt NPs vs. support in CO_2 hydrogenation, steady-state H_2/D_2 exchange experiments were performed under CO_2 hydrogenation conditions over UiO-67-Pt, Pt/Al_2O_3, Pt/SiO_2, UiO-67 and SiO_2. The transient evolution of the HD molecule following a feed switch from $CO_2 + H_2$ to $CO_2 + D_2$ is shown in Figure S9. Importantly, formation of HD (and other products) was observed only over the Pt containing materials but not over the UiO-67 and SiO_2 supports alone, showing that dissociation of H_2/D_2 only occurs when Pt is present. The amount of HD formed over UiO-67-Pt and Pt/Al_2O_3 was larger than over Pt/SiO_2, and in all cases 1–2 orders of magnitude higher than the amount of exposed Pt atoms in Pt nanoparticles (Table 1). This observation, in combination with the observed HD tailing, strongly suggests H/D exchange with hydroxyl groups on the support materials, either directly by hydrogen spillover to/from the Pt NPs, or by H/D exchange with the water molecules formed during reaction.

Insights into the origin of HD tailing and formed amount over the UiO-67-Pt sample were obtained by a parallel *operando* FT-IR experiment under comparable conditions (1 bar, 170 °C, $CO_2/H_2 = 1/6$). When exchanging H_2 for D_2, the sharp signal of Zr-μ_3-OH at 3669 cm^{-1} [39] decreased to zero with time while another equally sharp and intense peak, corresponding to the deuterated species Zr-μ_3-OD, increased at 2705 cm^{-1} (Figure S16). Interestingly, quantification of the molar number of H in HD, $N_{A,HD}$, yields 1200 μmol H per gram catalyst, which corresponds to about 70 % of the theoretical number of Zr-μ_3-OH groups in the sample. No other indication of H/D exchange (neither on Pt nor in linkers) was found from FT-IR experiments. More detailed description of the spectra obtained during FT-IR experiments over UiO-67-Pt, including the hydroxyl group region and the C-H bonds present in the aromatic linkers (carboxylates region is omitted as out of scale), is given in the supporting section (Figure S16).

Table 1. Pt amount, NP diameter (**d_{NP}**), CO-uptake (**$N_{A,CO,RT}$**), estimated exposed Pt surface (**$N_{surf,Pt}$**) and the amount of HD formed (**$N_{A,HD}$**) after switching from H_2+CO_2 to D_2+CO_2 at 170 °C, 1 bar.

Catalyst	**Pt amount** (wt %)	**d_{NP}** (nm)	**$N_{A,CO,RT}$**[c] (μmol/g_{cat})	**$N_{surf,Pt}$**[d] (μmol/g_{cat})	**$N_{A,HD}$** (μmol/g_{cat})
UiO-67-Pt	2.7[a]	3.6 ± 0.7	1.7 ± 0.3	55	1200
Pt/Al_2O_3	5[b]	1.4[b]	36	200	1100
Pt/SiO_2	5[b]	5 ± 2	13	76	540
Pt/C	5[b]	2[b]	-	-	-

[a]theoretical amount of impregnation. A Pt amount of 2.4 ± 0.4 wt % was estimated from EDX analysis (see SI). [b]obtained from the provider. [c]pulse-chemisorption at room temperature. [d]estimated from TEM by following the procedure described in the SI.

It is important to note that the chemical integrity of the catalyst is preserved during reaction and changes in the spectra are therefore caused by reaction products interacting with the sample. The most evident change is caused by the progressive increase of CO on the Pt nanoparticles (Figure 2). The shape and frequency of this signal is compatible with carbonyls linearly adsorbed on Pt atoms at the surface of NPs, as we already addressed in our previous study on an analogous material.[17] The size of the particles (3.6 nm) and the temperature (170 °C) justify the absence of bridged carbonyl species at lower frequencies. Changes in one of the smaller peaks in the IR spectra is the most novel observation of this study: the peak arising at 2745 cm^{-1} (Figure 2) is due to the appearance of bidentate formate groups[39] (which, notably, are absent after activation, see Figure 2) most likely coming from the progressive process of CO_2 reduction. The frequency of this weak feature is compatible with ν_s(COO) + δ(CH) vibration of bidentate formates directly connected to open Zr-sites of the Zr-nodes in the MOF framework.[39, 50, 51] Further bands associated to formate are visible in the top part of Figure S16 in the region 3000-2800 cm^{-1}. The spectrum of the sample collected during CO_2 hydrogenation after the subtraction of the activated one (Figure S17) highlights the formation of four additional bands at 2910, 2888, 2868 and 2854 cm^{-1}, ascribable to various formate species at the Zr-node.[39] This is to the best of our knowledge, the first report of formate formation at the MOF Zr-node under CO_2 hydrogenation reaction conditions.

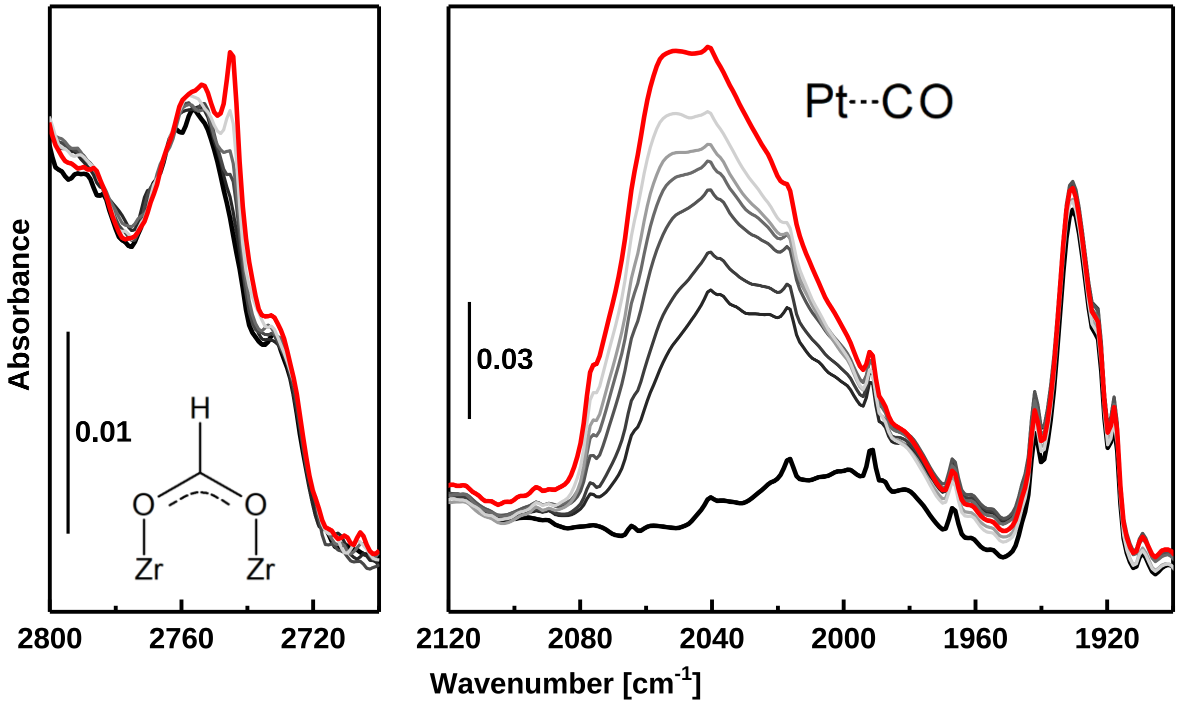

Figure 2. FT-IR spectra of UiO-67-Pt collected during CO_2 hydrogenation ($CO_2/H_2 = 1/6$, 10 ml/min, 170 °C, 1 bar) at different times (thick black curve for t = 0 min, grey scale from darkest to brightest for $0 < t < 120$ min, thick red curve for t = 120 min). The left figure shows the magnified spectral region of the ν(C-H) for formate groups, while the right figure depicts the spectral interval typical for CO linearly adsorbed on metal nanoparticles. Full range spectra are reported in Figure S16.

The importance of these moieties is even more evident, thanks to the isotopic exchange experiment between H_2 and D_2. When exchanging H_2 for D_2, the signals of the formate groups shifted to lower wavenumbers; the signals in the 2950–2850 cm^{-1} region shifted to the region of the CO_2 roto-vibrational profile and are therefore not detectable. Conversely, the band at 2745 cm^{-1} shifted to 2168 cm^{-1} [39] (Figure S16) and the intensity vastly increased as compared to the H-analogue ($I_{HCOO}/I_{DCOO} \approx 0.02$). The intensity increase indicates an inverse kinetic isotope effect, although possible differences in the extinction coefficient of the two species cannot be excluded. Importantly, a corresponding, gradual increase in methanol production rate was observed upon H_2/D_2 exchange under steady-state CO_2 hydrogenation conditions (Figure S14). At isotope equilibration, this difference in H- and D-methanol production rates corresponds to an inverse Kinetic Isotope Effect (KIE), $r_H/r_D = 0.36$. Moreover, the temporal scale of exchange was very similar for the formate species and for methanol in the parallel H_2/D_2 exchange experiments performed in the FT-IR transmission cell and the test-setup, respectively (Figure 3) (See Experimental section for details). Together, these experiments provide firm evidence that the Zr-formate species is a key intermediate in the methanol formation path.

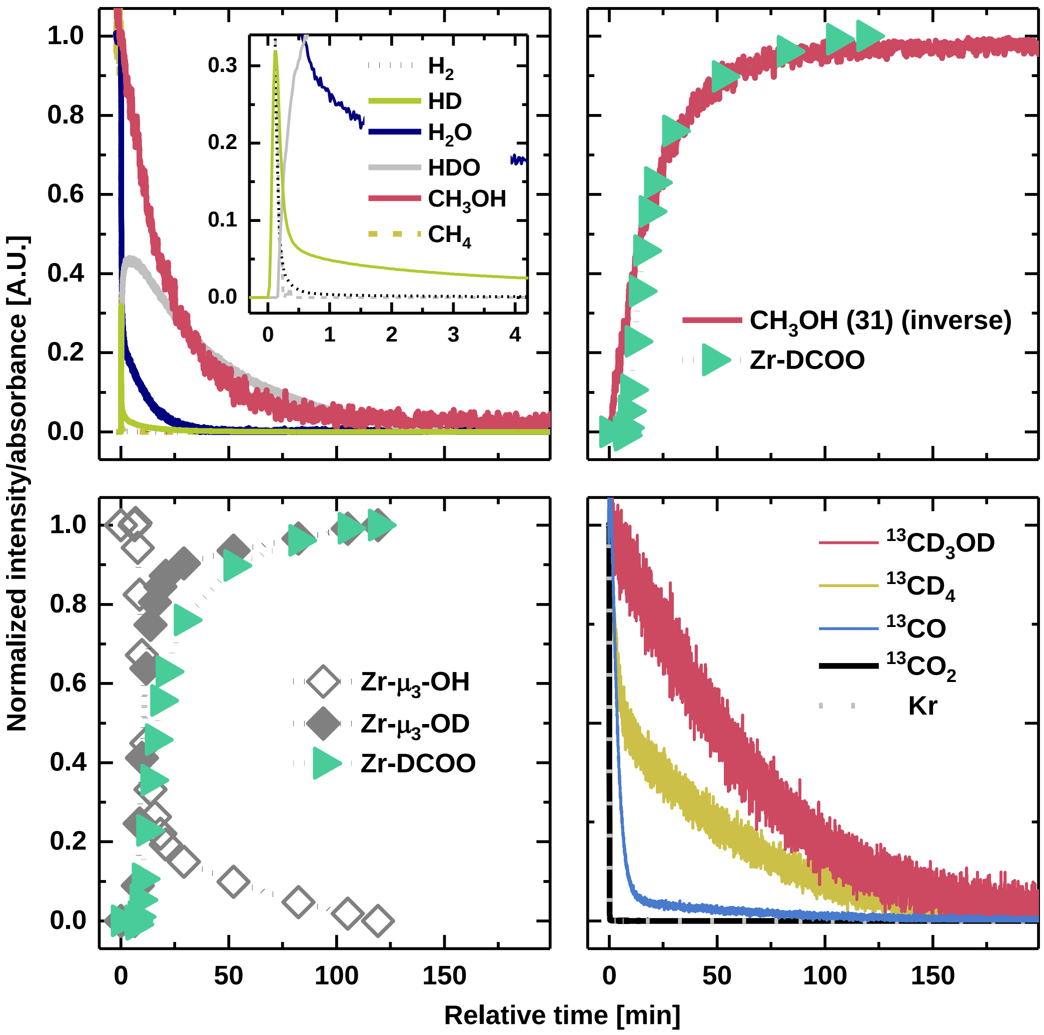

Figure 3. Top left: The normalized intensity of H_2 (m/z = 2), HD (m/z = 3), H_2O (m/z = 18), HDO (m/z = 19), CH_3OH (m/z = 31) and CH_4 (m/z =15) when switching from CO_2+H_2 to CO_2+D_2 at t = 0. Top right: Comparison of Zr-DCOO and CH_3OH (inverse) during H/D exchange. Bottom left: Normalized absorbance of Zr-μ$_3$OH (open diamonds), Zr-μ$_3$OD (filled diamonds) and deuterated formate (triangles) during exchange of H_2 to D_2 at steady state CO_2 hydrogenation. $CO_2/H_2(D_2)$ = 1/6, 10 ml/min, 170 °C, 1 bar. Bottom right: The normalized intensity of Kr (m/z = 84), $^{13}CO_2$ (m/z = 45), ^{13}CO (m/z = 29), $^{13}CD_4$ (m/z = 21) and $^{13}CD_3OD$ (m/z = 35) products when switching from $^{13}CO_2$ + D_2 to $^{12}CO_2$ + D_2 at t = 0. T = 170 °C, 1 bar, $\tau = 0.01\ g_{cat}\cdot$min/ml.

Furthermore, during a complementary ($^{13}CO_2$+D_2)/($^{12}CO_2$+D_2) exchange experiment (Figure 3), $^{13}CD_3OD$ decreased steadily to zero in about 200 minutes, similarly to what observed for formate and methanol during the H_2/D_2 switch. The slope of the normalized intensity of methanol in a semi logarithmic plot (Figure S15) is inversely proportional to the mean surface residence time ($-1/\tau_{res}$) of intermediates leading to the formation of methanol (Table 3), and is characteristic of formation from a single pool of intermediates.[52]

Overall, the transient experiments provide firm evidence that formate species, attached to the Zr nodes in a bidentate configuration, are formed by H transfer from an adjacent Pt NP. The inverse KIE observed for methanol formation ($r_H/r_D = 0.36$) is a signature of reactions where the rate limiting step involves hydrogen addition to an sp- or sp^2-hybridized carbon, leading to a hybridization change (sp to sp^2, or sp^2 to sp^3).[10, 53] CO_2 hydrogenation to methanol via formate species involves two such steps, CO_2 hydrogenation to form formate, and formate hydrogenation to (probably) form dioxymethylene. The observation of abundant formate species by FT-IR and by $^{13}C/^{12}C$ transient integration (Table 3) further suggest that hydrogenation of the formate species is the rate limiting step of methanol formation in UiO-67-Pt. Previously, an inverse KIE (albeit not as strong as in our case) was reported for CO_2 to methanol over $Cu/ZnO/Al_2O_3$, Cu/SiO_2, Cu/MgO and Pd/SiO_2.[10] In that case, DFT calculations predicted an inverse KIE for hydrogenation of the formate species, in line with our results. A schematic presentation of the postulated reaction mechanism is shown in Scheme 2.

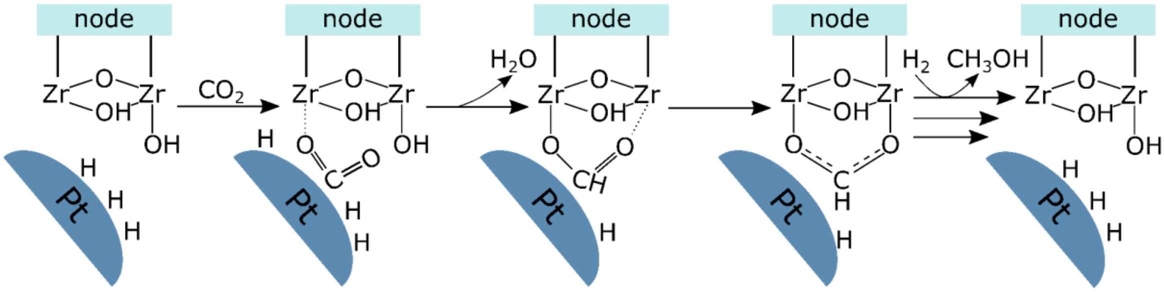

Scheme 2. Schematic presentation of the postulated reaction mechanism of CO_2 hydrogenation to the formate intermediate in CH_3OH formation at the Pt–Zr-node interface.

Integration of the $^{13}C/^{12}C$ transient response of methanol showed an intermediate species concentration of 23 μmol/g (Table 3), i.e. close to half the amount of Pt surface species estimated for the ensemble of Pt NPs identified by TEM (3.6 nm average diameter, Table 1). The schematic illustration of such a particle embedded in the MOF structure suggests that the average Pt NP contains 640 surface Pt sites, and is surrounded by 32 Zr nodes that have a total of 224 Zr-sites accessible for coordination at the Pt – MOF interface, corresponding to ~~84~~112 bidentate formate species (Scheme 1, Figure 2). These numbers yield a formate:Pt surface site ratio of 112:640 (0.2), substantially lower than the estimated 24:55 (0.4) ratio from transient experiments.

Importantly, the numbers imply that additional Zr-sites are available to formate formation around each Pt NP. In this respect, we hypothesized that Zr-sites might become accessible by breaking Zr-linker bonds, either during Pt NP formation, or during the catalytic reaction. The hypotheses were investigated by periodic Density Functional Theory (DFT) calculations. (See Experimental Details section for a brief description of the methodology and SI for further computational details and model construction). A Pt_{89} NP occupying the tetrahedral cavity of UiO-67

(Figure S18), $\mathbf{Pt_{89}^{tet}}$, was found to be an adequate model, justified by the assumption that the interface between the Pt NP and the linker/Zr node is similar when the NP has a diameter of 3.6 nm or ≈ 1 nm.

In the perfect MOF structure, all 24 coordination sites of each Zr-node are occupied by the carboxylate groups of the linker molecules (L). We first investigated the opening of such sites and computed the free energy profile of the system when a linker decoordinates from the node and slides along the Pt NP surface (Figure 4 and Figure S22). Decoordination of the linker presumably occurs via $\sigma(Csp^2\text{-}Csp^2)$-bond rotation at the $O_2C\text{-}C(Aryl)$ fragment, which generally involves low energy barriers. In Figure 4, L^X and O_2^X indicates the coordination mode of the linker or formate oxygen to the Zr-node (X= number of Zr-O bonds) and * indicates the atom adsorbed to the Pt_{89} NP. These calculations showed that it is unfavorable to open two Zr-sites ($\Delta G(L^2 \rightarrow L^0) = 16$ kJ/mol), while opening one Zr-site is favorable, $\Delta G(L^2 \rightarrow L^1) = -54$ kJ/mol). Considering next the catalytic reaction, the first step of formate formation is the adsorption of a CO_2 molecule which was found to coordinate its C atom to the Pt surface and the O atom to the opened Zr-site ($\Delta G_{ads}(L^1 + CO_2 \rightarrow \mathbf{C^*O_2^1}) = -20$ kJ/mol) (Figure 4). Continuing on the formate formation pathway from the $\mathbf{L^1\text{-}C^*O_2}$ intermediate, the two subsequent intermediates, $\mathbf{L^1\text{-}C^*O_2^1{+}2H^*}$, $\Delta G\ \mathbf{L^2 + CO_2 + H_2 \rightarrow L^1\text{-}C^*O_2^1{+}2H^*}) = -144$ kJ/mol and $\mathbf{L^1\text{-}HCO_2^1{+}H^*}$, $\Delta G(\mathbf{L^2 + CO_2 + H_2 \rightarrow L^1\text{-}HCO_2^1{+}H^*}) = -107$ kJ/mol, correspond to H_2 adsorption on the Pt NP and a formate + hydride species, respectively (Figure 4). The H_2 adsorption is exergonic by -70 kJ/mol, and the subsequent H transfer to the C atom of CO_2 is endergonic by 37 kJ/mol. Interestingly, the transformation from $\mathbf{L^1\text{-}HCO_2^1{+}H^*}$ to $\mathbf{L^0\text{-}HCO_2^2{+}H^*}$, $\Delta G(\mathbf{L^2 + CO_2 + H_2 \rightarrow L^0\text{-}HCO_2^2{+}H^*}) = -29$ kJ/mol, where the formate species is coordinated to two Zr-sites is highly endergonic, $\Delta G_r(\mathbf{L^1\text{-}HCO_2^1{+}H^* \rightarrow L^0\text{-}HCO_2^2{+}H^*}) = 78$ kJ/mol. The transformation from $\mathbf{L^1\text{-}HCO_2^1{+}H^*}$ to $\mathbf{L^0\text{-}HCO_2^2{+}H^*}$ comprises two structural changes: i) The formate moiety goes from being coordinating to one Zr-site to being coordinated to two Zr-sites; ii) the linker decoordinates from one Zr-site, opening two Zr-sites. To estimate the contribution to the free energy change, $\Delta G(\mathbf{L^1\text{-}HCO_2^1{+}H^* \rightarrow L^0\text{-}HCO_2^2{+}H^*})$, of i) and ii), a computational experiment was performed: while keeping the linker in a “completely open position” (L^0), the formate moiety was oriented to its Zr-monodentate configuration $\mathbf{HCO_2^1}$. This resulted in a potential energy increase of 45 kJ/mol.

These results indicate that the coordination of formate by one Zr-O bond (monodentate) is thermodynamically preferred in nodes initially saturated by linkers (L^2), while the coordination of formate by two Zr-O bonds (bidentate) is thermodynamically preferred in nodes initially having lost some linkers (L^0). Therefore, the observation of the latter coordination mode of formate by FT-IR suggests that these species have been generated in Zr nodes with empty coordination sites at the start of the reaction.

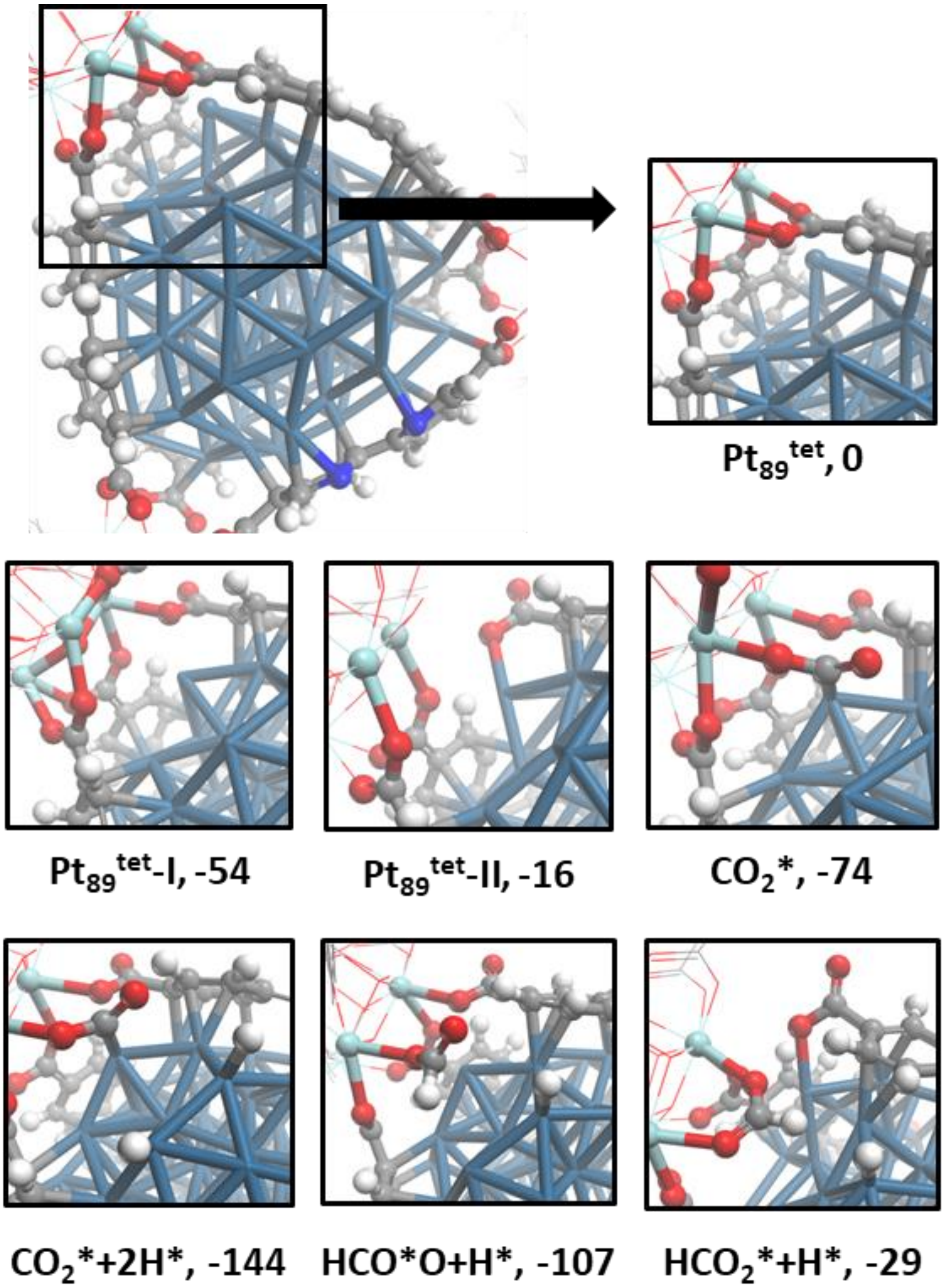

Pt_{89}^{tet}, 0

Pt_{89}^{tet}-I, -54

Pt_{89}^{tet}-II, -16

CO_2*, -74

CO_2*+2H*, -144

HCO*O+H*, -107

HCO_2*+H*, -29

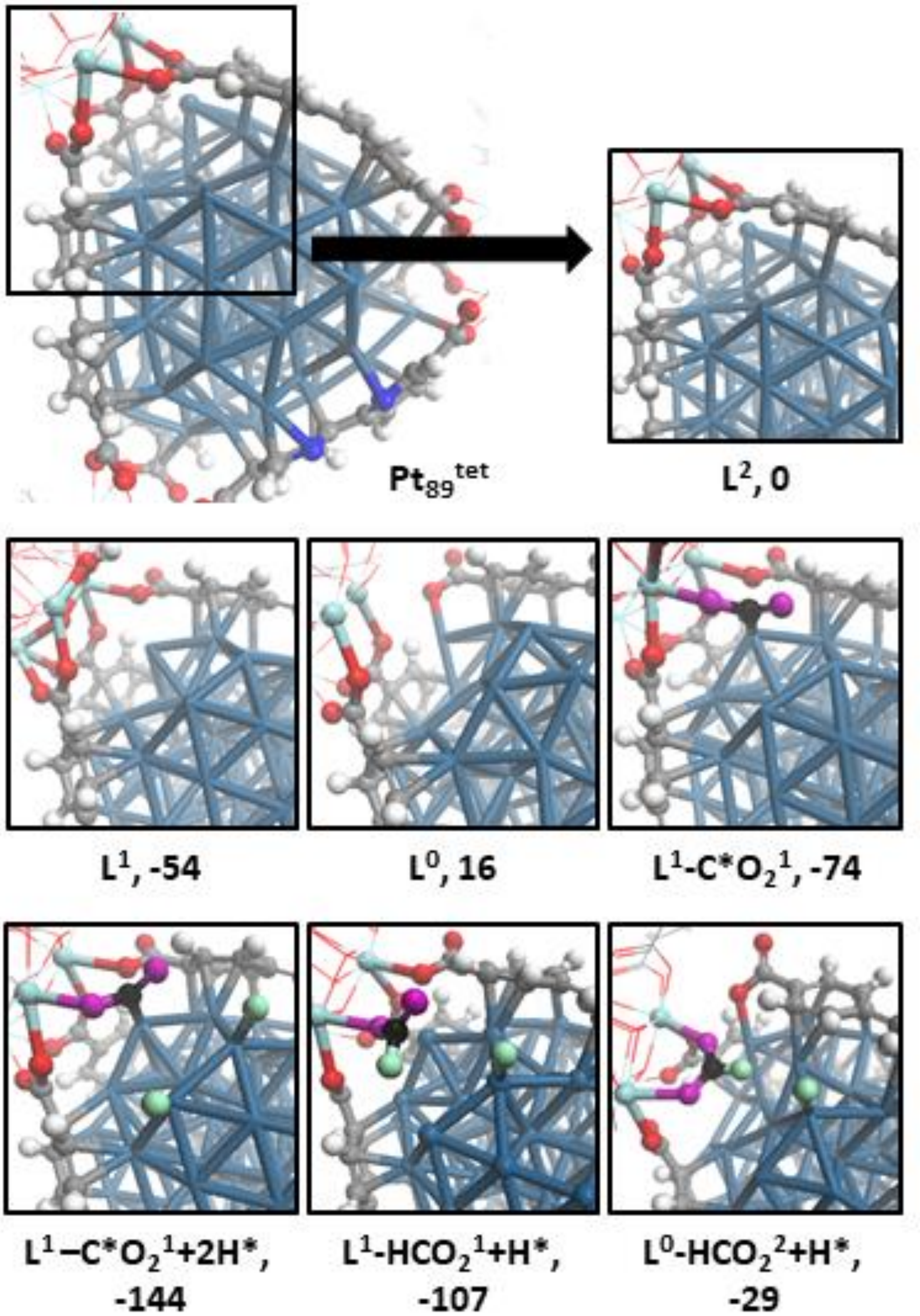

Figure 4. 3D representations of intermediates of the reaction pathway towards the formation of the formate species coordinated to two Zr sites. Values are free energies in kJ/mol. L^X and O_2^X indicates the coordination number of the linker and formate to the Zr-node, and * the atom adsorbed to Pt. O, C and H atoms from CO_2 and H_2 are in pink, black and green; and for the linker, in red, grey and white.

It was therefore explored whether the growth of the Pt NP during activation could cause the formation of such Zr nodes with open coordination sites. Insight into this possibility was obtained by computing the free energy of the Pt particle growth from $\mathbf{Pt_{55}}^{tet}$ to $\mathbf{Pt_{89}}^{tet}$. These calculations showed that the reaction free energy of the system decreases as the Pt NP grows, and the decrease in energy will eventually exceed the energy loss of linker detachment (Figure S19, Figure S20 and Figure S21). Thus, during the nanoparticle growth, linkers will detach from the Zr nodes, and the Zr nodes will decorate the growing Pt nanoparticle. Returning to Scheme 1, the number of Zr nodes that needs to be removed from a perfect MOF lattice in order to create the 3.6 nm model Pt NP is minimum 6. The corresponding number of additional bidentate formate sites is 54. In combination with the 112 formate sites of the surrounding framework bound nodes, this yields a total number of formate sites of 166 and a formate-to-Pt surface atom ratio of 0.3, in reasonable agreement with the experimentally observed numbers.

Support for the computational results were found from on-line Mass Spectrometry (MS) measurements performed during activation in 10% H_2/Ar atmosphere at 350 °C. The MS data revealed traces of phenyl-containing fragments in the effluent gas, suggesting that modulator and/or linker molecules desorbed from the material during Pt NP formation (Figure S8). The crystallographic features of the material were unchanged (Figure S2, Figure S5 and Figure S6) and the BPYDC/BPDC ratio remained constant during subsequent testing (Table S2). Furthermore, no linker fragments were observed during a second activation of UiO-67-Pt after testing, in line with the excellent catalyst stability observed under reaction conditions.

Having established the importance of the Zr-nodes and formate intermediates for methanol formation over UiO-67-Pt, the next issue is whether methanol formation could be decoupled from CO and CH_4 formation, hence, optionally leading to higher methanol selectivity. To this end, we first turn to classical kinetic experiments.

Contact time variation experiments, under otherwise constant conditions, showed that methanol selectivity is constant when CO_2 conversion increases, suggesting that it is a primary reaction product (Figure 5). Conversely, methane selectivity increases with increasing CO_2 conversion, while CO selectivity decreases, suggesting that CH_4 is mainly a secondary product, formed via CO. The latter result is in accordance with our previous studies of an analogous catalyst at higher temperature.[17]

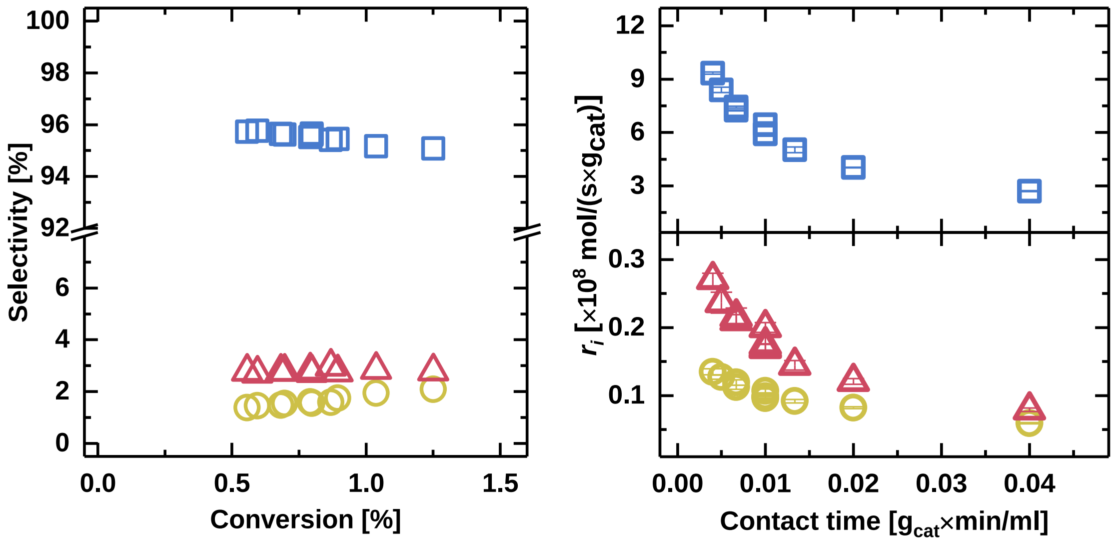

Figure 5. Contact time variation during CO_2 hydrogenation to CO (squares), CH_4 (circles) and CH_3OH (triangles) at 170 °C, 1 bar, $CO_2/H_2/He$ = 1/6/3 and τ = 0.004–0.04 g_{cat}·min/ml. Left: Selectivity versus conversion. Right: Rate of product formation versus contact time.

Next, partial pressure variation experiments were performed in order to assess reaction orders for each product. This assessment was complicated by the decreased formation rate of all products with increasing contact time (Figure 5), indicating strong adsorption of one or several reaction products, thereby poisoning the active site(s).[10, 19] Indeed, when correlating the rate decrease with the partial pressures of the majority products, CO and H_2O, all products have a reaction order close to negative 1 in p(CO+H_2O), CH_4 slightly less negative (Figure S10 and Table 2). Based on FT-IR results reported above, showing that CO adsorbed on Pt (2042 cm^{-1})[17] dominates the Pt surface under the respective reaction conditions, CO was assessed as the main contributor to the inhibition, likely suppressing the coverage in H[8] by competitive adsorption. When taking into account the variable concentration of CO and H_2O, positive reaction orders in pH_2 and pCO_2 were observed for all products, but with substantial differences (Table 2).

Considering first the majority product, CO, its formation rate depends strongly on P(CO_2), but less on p(H_2) (Table 2). Furthermore, no Kinetic Isotope Effect (KIE) was observed for CO during the (CO_2+H_2)/(CO_2+D_2) transient experiment (Table S5 and Figure S14), showing that breaking or making of H-H or H-O bonds (which would otherwise lead to a primary KIE)[10, 54] is not rate-determining for CO formation under the conditions studied here. Finally, the number of surface intermediates leading to CO formation and their mean residence time were calculated from the $^{13}C/^{12}C$ transients (Table 3 and Figure 3). The normalized ^{13}CO signal rapidly decreased to around 0.05 within the first 15 minutes then slowly reached zero in the following 150 minutes. It is interesting to note that the number of surface intermediates leading to CO formation represents half of the Pt surface atoms in Pt NPs, estimated from TEM measurements (Table 1 vs. Table 3). This observation, in combination with the partial coverage of the Pt NPs by Zr-nodes (and linkers), the inhibiting effect of CO, the high predicted barrier of CO desorption from Pt,[18] and the observation of a positive correlation between facile CO desorption and rate of CO formation in our previous study,[17] strongly suggest CO desorption as rate-limiting step in the RWGS reaction over UiO-67-Pt.

Table 2. Reaction orders in total pressure (p_{total}), and in pH_2, pCO_2 and $p(CO+H_2O)$ (1 bar) for the rate of conversion (X) and CO, CH_4 and CH_3OH formation at 170 °C over UiO-67-Pt.

p_i	X	CO	CH_4	CH_3OH
P_{total}	0.1	0	0.3	1.1
$CO+H_2O^a$	-1.1	-1.1	-0.7	-1
H_2^b	0.2	0.2	0.9	1.7
CO_2^b	0.9	0.9	0.1	0.7

[a] Estimated from contact time variation experiments (Figure 5 and Figure S10). The reaction orders represent the average of two experiments. [b] Reaction orders when taking into account variable pCO and pH_2O in the reactor.

Turning next to methane formation rate, it depends strongly on $P(H_2)$ and weakly on $P(CO_2)$ (Table 2). Considering the high coverage of CO, as well as the presumed indirect formation of methane via CO, this result is not surprising. In the $(CO_2+H_2)/(CO_2 + D_2)$ transient experiment, an inverse KIE of 0.6, i.e. intermediate between CO (KIE = 1) and methanol (KIE = 0.36), was observed for methane (Table S5 and Figure S14). Intriguingly, the inverse KIE was installed within the 15 minutes resolution of the gas analysis, hence, much more rapid than the transient behavior of methanol (Figure S14). Thus, the rate-determining step of methane formation involves bonding with hydrogen,[54-57] but the rate-determining step is not the same as for methanol formation. Indeed, the much more rapid transient behavior of methane compared to formate, disqualifies formate as a significant intermediate to methane formation. This result implies that, except for hydrogen activation, methane formation is mechanistically decoupled from methanol formation. The normalized CH_4 formation rate (represented by the m/z = 15 signal of CH_3) also decreases rapidly to zero (comparable to H_2) during the H/D exchange (Figure 3). Due to their mass overlap with the much more abundant water fragments, the time evolution of partially exchanged methane/methyl species could not be followed. The transient behavior of methane during the $^{13}C/^{12}C$ switch (Figure 3) was markedly different from that observed in the H/D transient: The normalized $^{13}CD_4$ formation rate decreased to 0.5 during the first 7 minutes and then slowly to zero in the following 160 minutes. This distinct shape of the isotope transient indicates methane formation from two pools in parallel,[52, 58] one rapidly converted to products and the other more slowly. Integration of the transient curve showed that the number of surface intermediates leading to methane formation is low (Table 3). Moreover, about 3%

of the methane-forming intermediates react fast and is responsible for about 50 % of the steady-state methane formation rate, while the other 97 % react slowly (Table 3 and Figure S15).

Returning finally to methanol, its formation depends strongly on both reactant partial pressures, in line with the observation that it is a primary product, formed independently of CO (Figure 5). The $^{13}C/^{12}C$ transient experiment shows that methanol is formed from a similar number of surface intermediates as CO, but their turn-over rate is much slower, hence leading to the 9 % methanol selectivity observed under the respective conditions (Table 3).

Table 3. Mean surface residence times τ_{res} and the number N_{ad} of surface intermediates leading to the formation of ^{13}CO, $^{13}CD_4$ and $^{13}CD_3OD$ at 170 °C (1 bar), calculated from integration of the curves in Figure 3 and the isotope-independent steady-state reaction rates.

	INT(CO)	**INT(CD_4)**	**INT(CD_3OD)**
$\mathbf{N_{ads}}$ ($\mu mol/g_{cat}$)	~~31~~ 26 ± 3	~~3.2~~ 3 ± 0.3	~~24~~23 ± 2
$\boldsymbol{\tau_{res}}$ (s)	~~540~~ 0.5×10^3	~~2174~~ 2.1×10^3	~~3897~~ 3.8×10^3

Considering finally the non-carbon products HD, H_2O and HDO, they exhibited slow or partially slow transient responses (Figure 3). HD has a sharp initial peak with considerable tailing over the course of the following hour, indicating formation from parallel pools and/or exchange with hydrogen-containing surface species.[59] H_2O showed transient characteristics suggestive of parallel pools, similar to CO and CH_4, and the HDO signal increased rapidly to a maximum within a few minutes then slowly decreased over the course of 2 hours, closely following the methanol signal. The long surface lifetime of these products is indicative of a long-lived source of H participating in their formation, presumably also in the formation of methanol. Interestingly, quantification of the mol H in HD, H_2O, HDO and CH_3OH yields 1500 μmol H per gram catalyst, which corresponds to about 80 % of the theoretical amount of mol Zr μ_3-OH groups in the sample (HD accounts for 70 %, as reported above).

Conclusion

Mechanistic aspects of CO_2 hydrogenation over UiO-67-Pt and the role of the UiO-67 framework have been investigated in detail by employment of steady-state and transient kinetic studies, coupled with *operando* infrared spectroscopy and DFT modeling.

It was observed that Pt NPs embedded in the MOF structure are responsible for hydrogen activation, and that formate species are formed at the Zr nodes by reaction between adsorbed CO_2 and hydrogen spill-over from an adjacent Pt NP. These results demonstrate that the Pt NPs strongly interact with defect Zr nodes during reaction, and hence, that Zr nodes decorate the surface of the Pt

NPs. Formate species are the most abundant intermediates in the reaction path to methanol, and transient results suggest that formate hydrogenation is the rate-limiting step of methanol formation. Importantly, the abundance of formate species is limited by the number of Zr sites made available by linker detachment due to Pt NP growth during catalyst activation.

CO and methane formation are mechanistically separated from methanol formation, except for the hydrogen dissociation step. The main route to methane formation is proposed as CO hydrogenation. Moreover, the presented data are consistent with CO desorption being the rate limiting step of the reverse water gas shift reaction over UiO-67-Pt.

Acknowledgement

E.S.G, A.L., G.K., S.Ø.-Ø., S.B., S.S., K.P.L. and U.O. acknowledge the Research Council of Norway for financial support (FRINATEK ToppForsk Grant No. 250795 CONFINE). We further acknowledge Chimet for providing Pt/Al_2O_3 and Pt/C catalysts.

T.F. acknowledge the Norwegian Metacenter for Computational Science (NOTUR) for computational resources (projects number nn4654k and nn4683k), Michele Cacella for useful advice on the methodology, Sri Harsha Pulumati for fruitful discussions, Jingyun Ye and J. Karl Johnson for help with reproducing their calculations of reference [53].

T.F., E.S. and A.N. acknowledge support by the 'Nordic Consortium for CO2 Conversion' (NordForsk project No. 85378, site.uit.no/nordco2).

A. N. acknowledge the support from the Research Council of Norway (FRINATEK Grant No. 250044 and Center of Excellence Grant No. 262695).

Author Information

Corresponding Author

*unni.olsbye@kjemi.uio.no

Associated Content

Supporting Information

Catalyst preparation, characterization, catalytic testing, operando FTIR and computational details.

References

1. Bellotti, D.; Rivarolo, M.; Magistri, L.; Massardo, A. F., Feasibility study of methanol production plant from hydrogen and captured carbon dioxide. *J. CO2 Util.* **2017,** *21*, 132-138.
2. Chu, S.; Cui, Y.; Liu, N., The path towards sustainable energy. *Nat. Mater.* **2016,** *16*, 16.

3. Olah, G. A., Beyond Oil and Gas: The Methanol Economy. *Angew. Chem. Int. Ed* **2005,** *44* (18), 2636-2639.

4. Porosoff, M. D.; Yan, B.; Chen, J. G., Catalytic reduction of CO2 by H2 for synthesis of CO, methanol and hydrocarbons: challenges and opportunities. *Energy Environ. Sci.* **2016,** *9* (1), 62-73.

5. Wang, W.; Wang, S.; Ma, X.; Gong, J., Recent advances in catalytic hydrogenation of carbon dioxide. *Chem. Soc. Rev.* **2011,** *40* (7), 3703-3727.

6. Li, W.; Wang, H.; Jiang, X.; Zhu, J.; Liu, Z.; Guo, X.; Song, C., A short review of recent advances in CO2 hydrogenation to hydrocarbons over heterogeneous catalysts. *RSC Adv.* **2018,** *8* (14), 7651-7669.

7. Kattel, S.; Liu, P.; Chen, J. G., Tuning Selectivity of CO2 Hydrogenation Reactions at the Metal/Oxide Interface. *J. Am. Chem. Soc.* **2017,** *139* (29), 9739-9754.

8. Wang, X.; Shi, H.; Kwak, J. H.; Szanyi, J., Mechanism of CO2 Hydrogenation on Pd/Al2O3 Catalysts: Kinetics and Transient DRIFTS-MS Studies. *ACS Catal.* **2015,** *5* (11), 6337-6349.

9. Wu, H. C.; Chang, Y. C.; Wu, J. H.; Lin, J. H.; Lin, I. K.; Chen, C. S., Methanation of CO2 and reverse water gas shift reactions on Ni/SiO2 catalysts: the influence of particle size on selectivity and reaction pathway. *Catal. Sci. Technol.* **2015,** *5* (8), 4154-4163.

10. Kunkes, E. L.; Studt, F.; Abild-Pedersen, F.; Schlögl, R.; Behrens, M., Hydrogenation of CO2 to methanol and CO on Cu/ZnO/Al2O3: Is there a common intermediate or not? *J. Catal.* **2015,** *328*, 43-48.

11. Chen, X.; Su, X.; Duan, H.; Liang, B.; Huang, Y.; Zhang, T., Catalytic performance of the Pt/TiO2 catalysts in reverse water gas shift reaction: Controlled product selectivity and a mechanism study. *Catal. Today* **2017,** *281*, 312-318.

12. Hartadi, Y.; Widmann, D.; Behm, R. J., Methanol formation by CO2 hydrogenation on Au/ZnO catalysts – Effect of total pressure and influence of CO on the reaction characteristics. *J. Catal.* **2016,** *333*, 238-250.

13. Gaikwad, R.; Bansode, A.; Urakawa, A., High-pressure advantages in stoichiometric hydrogenation of carbon dioxide to methanol. *J. Catal.* **2016,** *343*, 127-132.

14. Román-Martínez, M. C.; Cazorla-Amorós, D.; Linares-Solano, A.; Salinas-Martínez de Lecea, C., CO2 hydrogenation under pressure on catalysts Pt ・ Ca/C. *Appl. Catal., A* **1996,** *134* (1), 159-167.

15. Kim, S. S.; Park, K. H.; Hong, S. C., A study of the selectivity of the reverse water–gas-shift reaction over Pt/TiO2 catalysts. *Fuel Process. Technol.* **2013,** *108*, 47-54.

16. Goguet, A.; Meunier, F. C.; Tibiletti, D.; Breen, J. P.; Burch, R., Spectrokinetic investigation of reverse water-gas-shift reaction intermediates over a Pt/CeO2 catalyst. *J. Phys. Chem. B* **2004,** *108* (52), 20240-20246.

17. Gutterød, E. S.; Øien-Ødegaard, S.; Bossers, K.; Nieuwelink, A.-E.; Manzoli, M.; Braglia, L.; Lazzarini, A.; Borfecchia, E.; Ahmadigoltapeh, S.; Bouchevreau, B.; Lønstad-Bleken, B. T.; Henry, R.; Lamberti, C.; Bordiga, S.; Weckhuysen, B. M.; Lillerud, K. P.; Olsbye, U., CO2 Hydrogenation over Pt-Containing UiO-67 Zr-MOFs—The Base Case. *Ind. Eng. Chem. Res.* **2017,** *56* (45), 13206-13218.

18. Kattel, S.; Yan, B.; Chen, J. G.; Liu, P., CO2 hydrogenation on Pt, Pt/SiO2 and Pt/TiO2: Importance of synergy between Pt and oxide support. *J. Catal.* **2016,** *343*, 115-126.

19. Kim, S. S.; Lee, H. H.; Hong, S. C., A study on the effect of support's reducibility on the reverse water-gas shift reaction over Pt catalysts. *Appl. Catal., A* **2012,** *423*, 100-107.

20. Tibiletti, D.; Goguet, A.; Meunier, F. C.; Breen, J. P.; Burch, R., On the importance of steady-state isotopic techniques for the investigation of the mechanism of the reverse water-gas-shift reaction. *Chem. Commun.* **2004,** (14), 1636-1637.

21. Jacobs, G.; Davis, B. H., Reverse water-gas shift reaction: steady state isotope switching study of the reverse water-gas shift reaction using in situ DRIFTS and a Pt/ceria catalyst. *Appl. Catal., A* **2005,** *284* (1), 31-38.

22. Kalamaras, C. M.; Panagiotopoulou, P.; Kondarides, D. I.; Efstathiou, A. M., Kinetic and mechanistic studies of the water–gas shift reaction on Pt/TiO2 catalyst. *J. Catal.* **2009,** *264* (2), 117-129.

23. Burch, R.; Goguet, A.; Meunier, F. C., A critical analysis of the experimental evidence for and against a formate mechanism for high activity water-gas shift catalysts. *Appl. Catal., A* **2011,** *409-410*, 3-12.

24. Kalamaras, C. M.; Olympiou, G. G.; Efstathiou, A. M., The water-gas shift reaction on Pt/γ-Al2O3 catalyst: Operando SSITKA-DRIFTS-mass spectroscopy studies. *Catal. Today* **2008,** *138* (3), 228-234.

25. Ouyang, B.; Xiong, S.; Zhang, Y.; Liu, B.; Li, J., The study of morphology effect of Pt/Co3O4 catalysts for higher alcohol synthesis from CO2 hydrogenation. *Appl. Catal., A* **2017,** *543*, 189-195.

26. Sápi, A.; Rajkumar, T.; Ábel, M.; Efremova, A.; Grósz, A.; Gyuris, A.; Ábrahámné, K. B.; Szenti, I.; Kiss, J.; Varga, T.; Kukovecz, Á.; Kónya, Z., Noble-metal-free and Pt nanoparticles-loaded, mesoporous oxides as efficient catalysts for CO2 hydrogenation and dry reforming with methane. *J. CO2 Util.* **2019,** *32*, 106-118.

27. Liu, B.; Ouyang, B.; Zhang, Y.; Lv, K.; Li, Q.; Ding, Y.; Li, J., Effects of mesoporous structure and Pt promoter on the activity of Co-based catalysts in low-temperature CO2 hydrogenation for higher alcohol synthesis. *J. Catal.* **2018,** *366*, 91-97.

28. Inoue, T.; Iizuka, T., Hydrogenation of carbon dioxide and carbon monoxide over supported platinum catalysts. *J. Chem. Soc., Faraday Trans. 1* **1986,** *82* (6), 1681-1686.

29. Rungtaweevoranit, B.; Baek, J.; Araujo, J. R.; Archanjo, B. S.; Choi, K. M.; Yaghi, O. M.; Somorjai, G. A., Copper Nanocrystals Encapsulated in Zr-based Metal–Organic Frameworks for Highly Selective CO2 Hydrogenation to Methanol. *Nano Lett.* **2016,** *16* (12), 7645-7649.

30. An, B.; Zhang, J.; Cheng, K.; Ji, P.; Wang, C.; Lin, W., Confinement of Ultrasmall Cu/ZnOx Nanoparticles in Metal–Organic Frameworks for Selective Methanol Synthesis from Catalytic Hydrogenation of CO2. *J. Am. Chem. Soc.* **2017,** *139* (10), 3834-3840.

31. Lippert, G.; Hutter, J.; Parrinello, M., The Gaussian and augmented-plane-wave density functional method for ab initio molecular dynamics simulations. *Theor. Chem. Acc.* **1999,** *103*, 124-140.

32. Lippert, G.; Hutter, J.; Parrinello, M., A hybrid Gaussian and plane wave density functional scheme. *Mol. Phys.* **1997,** *92* (3), 477-487.

33. VandeVondele, J.; Krack, M.; Mohamed, F., Quickstep: Fast and accurate density functional calculations using a mixed Gaussian and plane waves approach. *Comput. Phys. Commun.* **2005,** *167*, 103-128.

34. Group, C. K. D. *CP2K*, version 6.1; 2018.

35. Hutter, J.; Iannuzzi, M.; Schiffmann, F.; VandeVondele, J., CP2K: atomistic simulations of condensed matter systems. *WIREs Comput. Mol. Sci.* **2014,** *4*, 15-25.

36. VandeVondele, J.; Hutter, J., Gaussian basis sets for accurate calculations on molecular systems in gas and condensed phases. **2007,** *127* (11), 114105.

37. Kaur, G.; Øien-Ødegaard, S.; Lazzarini, A.; Chavan, S. M.; Bordiga, S.; Lillerud, K. P.; Olsbye, U., Controlling the Synthesis of Metal–Organic Framework UiO-67 by Tuning Its Kinetic Driving Force. *Cryst. Growth Des.* **2019,** *19* (8), 4246-4251.

38. Wu, H.; Chua, Y. S.; Krungleviciute, V.; Tyagi, M.; Chen, P.; Yildirim, T.; Zhou, W., Unusual and Highly Tunable Missing-Linker Defects in Zirconium Metal–Organic Framework UiO-66 and Their Important Effects on Gas Adsorption. *J. Am. Chem. Soc.* **2013,** *135* (28), 10525-10532.

39. Yang, D.; Ortuño, M. A.; Bernales, V.; Cramer, C. J.; Gagliardi, L.; Gates, B. C., Structure and Dynamics of Zr6O8 Metal–Organic Framework Node Surfaces Probed with Ethanol Dehydration as a Catalytic Test Reaction. *J. Am. Chem. Soc.* **2018,** *140* (10), 3751-3759.

40. Shearer, G. C.; Chavan, S.; Bordiga, S.; Svelle, S.; Olsbye, U.; Lillerud, K. P., Defect Engineering: Tuning the Porosity and Composition of the Metal–Organic Framework UiO-66 via Modulated Synthesis. *Chem. Mater.* **2016,** *28* (11), 3749-3761.

41. Feng, L.; Yuan, S.; Zhang, L.-L.; Tan, K.; Li, J.-L.; Kirchon, A.; Liu, L.-M.; Zhang, P.; Han, Y.; Chabal, Y. J.; Zhou, H.-C., Creating Hierarchical Pores by Controlled Linker Thermolysis in Multivariate Metal–Organic Frameworks. *J. Am. Chem. Soc.* **2018,** *140* (6), 2363-2372.

42. Shearer, G. C.; Chavan, S.; Ethiraj, J.; Vitillo, J. G.; Svelle, S.; Olsbye, U.; Lamberti, C.; Bordiga, S.; Lillerud, K. P., Tuned to Perfection: Ironing Out the Defects in Metal–Organic Framework UiO-66. *Chem. Mater.* **2014,** *26* (14), 4068-4071.

43. Shearer, G. C.; Forselv, S.; Chavan, S.; Bordiga, S.; Mathisen, K.; Bjørgen, M.; Svelle, S.; Lillerud, K. P., In Situ Infrared Spectroscopic and Gravimetric Characterisation of the Solvent Removal and Dehydroxylation of the Metal Organic Frameworks UiO-66 and UiO-67. *Top. Catal.* **2013,** *56* (9), 770-782.

44. Trickett, C. A.; Gagnon, K. J.; Lee, S.; Gándara, F.; Bürgi, H.-B.; Yaghi, O. M., Definitive Molecular Level Characterization of Defects in UiO-66 Crystals. *Angew. Chem. Int. Ed* **2015,** *54* (38), 11162-11167.

45. Øien, S.; Wragg, D.; Reinsch, H.; Svelle, S.; Bordiga, S.; Lamberti, C.; Lillerud, K. P., Detailed Structure Analysis of Atomic Positions and Defects in Zirconium Metal–Organic Frameworks. *Cryst. Growth Des.* **2014,** *14* (11), 5370-5372.

46. Braglia, L.; Borfecchia, E.; Lomachenko, K. A.; Bugaev, A. L.; Guda, A. A.; Soldatov, A. V.; Bleken, B. T. L.; Oien, S.; Olsbye, U.; Lillerud, K. P.; Bordiga, S.; Agostini, G.; Manzoli, M.; Lamberti, C., Tuning Pt and Cu sites population inside functionalized UiO-67 MOF by controlling activation conditions. *Faraday Discuss.* **2017**.

47. Øien, S.; Agostini, G.; Svelle, S.; Borfecchia, E.; Lomachenko, K. A.; Mino, L.; Gallo, E.; Bordiga, S.; Olsbye, U.; Lillerud, K. P.; Lamberti, C., Probing Reactive Platinum Sites in UiO-67 Zirconium Metal–Organic Frameworks. *Chem. Mater.* **2015,** *27* (3), 1042-1056.

48. Braglia, L.; Borfecchia, E.; Martini, A.; Bugaev, A. L.; Soldatov, A. V.; Øien-Ødegaard, S.; Lønstad-Bleken, B. T.; Olsbye, U.; Lillerud, K. P.; Lomachenko, K. A.; Agostini, G.; Manzoli, M.; Lamberti, C., The duality of UiO-67-Pt MOFs: connecting treatment conditions and encapsulated Pt species by operando XAS. *Phys. Chem. Chem. Phys.* **2017,** *19* (40), 27489-27507.

49. Wang, X.; Shi, H.; Szanyi, J., Controlling selectivities in CO2 reduction through mechanistic understanding. *Nat. Commun.* **2017,** *8* (1), 513.

50. Busca, G.; Lamotte, J.; Lavalley, J. C.; Lorenzelli, V., FT-IR study of the adsorption and transformation of formaldehyde on oxide surfaces. *J. Am. Chem. Soc.* **1987,** *109* (17), 5197-5202.

51. Tibiletti, D.; Meunier, F. C.; Goguet, A.; Reid, D.; Burch, R.; Boaro, M.; Vicario, M.; Trovarelli, A., An investigation of possible mechanisms for the water–gas shift reaction over a ZrO2-supported Pt catalyst. *J. Catal.* **2006,** *244* (2), 183-191.

52. Ledesma, C.; Yang, J.; Chen, D.; Holmen, A., Recent Approaches in Mechanistic and Kinetic Studies of Catalytic Reactions Using SSITKA Technique. *ACS Catal.* **2014,** *4* (12), 4527-4547.

53. Lowry, T. H.; Richardson, K. S., *Mechanism and Theory in Organic Chemistry*. Harper & Row: 1987.

54. Ojeda, M.; Li, A.; Nabar, R.; Nilekar, A. U.; Mavrikakis, M.; Iglesia, E., Kinetically Relevant Steps and H2/D2 Isotope Effects in Fischer−Tropsch Synthesis on Fe and Co Catalysts. *J. Phys. Chem. C* **2010,** *114* (46), 19761-19770.

55. Watson, D. T. P.; Ge, Q.; King, D. A., Facile H–D exchange in adsorbed methylidyne on Pt{110}–(1×2) and deuteration to gaseous methane. *J. Chem. Phys.* **2001,** *115* (24), 11306-11316.

56. Polanyi, M., Reaction Rates of the Hydrogen Isotopes. *Nature* **1934,** *133*, 26.

57. Bawn, C. E. H.; Ogden, G., Wave mechanical effects and the reactivity of the hydrogen isotopes. *Trans. Faraday Soc.* **1934,** *30* (0), 432-443.

58. Shannon, S. L.; Goodwin, J. G., Characterization of Catalytic Surfaces by Isotopic-Transient Kinetics during Steady-State Reaction. *Chem. Rev.* **1995,** *95* (3), 677-695.

59. Xie, J.; Yang, J.; Dugulan, A. I.; Holmen, A.; Chen, D.; de Jong, K. P.; Louwerse, M. J., Size and Promoter Effects in Supported Iron Fischer–Tropsch Catalysts: Insights from Experiment and Theory. *ACS Catal.* **2016,** *6* (5), 3147-3157.

Supporting Information

Hydrogenation of CO_2 to Methanol by Pt Nanoparticles Encapsulated in UiO-67: Deciphering the Role of the MOF

Emil S. Gutterød[a], Andrea Lazzarini[a], Torstein Fjermestad[b], Gurpreet Kaur[a], Maela Manzoli[c], Silvia Bordiga[a,d], Stian Svelle[a], Karl P. Lillerud[a], Egill Skúlason[e], Sigurd Øien-Ødegaard[a], Ainara Nova[b], Unni Olsbye[a]*

[a]Centre for Materials Science and Nanotechnology, Department of Chemistry, University of Oslo, Sem Saelandsvei 26, N-0315 Oslo, Norway

[b]Hylleraas Centre for Quantum Molecular Sciences, Department of Chemistry, University of Oslo, P.O. Box 1033, Blindern, N-0315 Oslo, Norway

[c]Department of Drug Science and Technology and NIS - Centre for Nanostructured Interfaces and Surfaces, University of Turin, Via P. Giuria 9, Turin 10125, Italy

[d]Department of Chemistry, NIS Interdepartmental Centre and INSRM reference centre, University of Turin, via Quarello 15A, I-10135 Turin, Italy

[e]Science Institute and Faculty of Industrial Engineering, Mechanical Engineering and Computer Science, University of Iceland, VR-III, 107 Reykjavik, Iceland

S1. Catalyst Preparation

UiO-67-Pt

Samples of UiO-67-Pt were prepared by the following procedure: 135 g of $ZrCl_4$ (1 eq.) was added to a 3 l reactor containing 63 ml distilled water (6 eq.) and 2243 ml dimethylformamide (DMF) (50 eq.) held at room temperature on a stirring plate. The solution was heated to 80 °C and 212 g of benzoic acid (3 eq.) was added. When the benzoic acid was completely dissolved, 14 g 2,2'-bipyridine-5,5'-dicarboxylic acid (BPYDC) was added, followed by 126 g 1,1'-biphenyl-4,4'-dicarboxylic acid (BPDC). The resulting solution was heated overnight at 130 °C in a jacketed glass reactor (with stirring) equipped with a reflux condenser. The resulting product was isolated by filtration, washed with hot DMF (500 ml) and acetone (1 l) on the filter, and then dried at 150 °C in air overnight.

The MOF was then impregnated with K_2PtCl_4 (Sigma-Aldrich) in DMF at 100 °C overnight (with stirring) (details in ref. [1]). This procedure leads to the formation of well-defined BPYDC-$PtCl_2$

sites.[1] The amount K_2PtCl_4 used for the impregnation corresponded to a 2:1 BPYDC:Pt molar ratio and 2.7 wt % Pt in the final material.

Pt on Al_2O_3, SiO_2 and C

Pre-reduced 5 % Pt/Al_2O_3 and 5 % Pt/C were provided by Chimet.

Pre-reduced 5 % Pt/SiO_2 (Escat 2351) was purchased from abcr.

Characterization

The crystallinity and porosity of the prepared material, both before and after Pt-functionalization, was determined by powder X-ray diffraction (XRD) (Bruker D8 Discover, Cu kα, Lynx Eye silicon detector) and N_2 adsorption at 77 K (BELSORP mini-II), respectively.

The relative amounts of organic species capping the Zr-cluster were determined using solution state proton nuclear magnetic resonance (^{1}H-NMR) after dissolving the sample in NaOD/D_2O.[1]

Thermogravimetric analysis was performed on a Netzsch STA 449 F3-Jupiter instrument. Approximately 20 mg of sample was heated (in an Al_2O_3 sample holder) from 30 to 800 °C (5 °C/min) in flow of 5 ml/min O_2 and 20 ml/min of N_2. The platinum particle size distribution was determined by TEM (Jeol 3010-UHR), counting more than 1000 particles, and the accessible Pt surface was quantified by CO pulse chemisorption.[1]

The Pt/Zr ratio was estimated from energy-dispersive X-ray (EDX) analysis using a Hitachi SU8230 field emission scanning electron microscope (FESEM) with an XFlash 6|10 EDX detector. Powder samples of UiO-67-Pt was sputter coated with gold prior to the analysis. The average Pt/Zr ratio was 0.042 ± 0.002. Combining this with the results from TGA and ^{1}H-NMR (*vide infra*), the wt % is estimated from the stoichiometric formula $Zr_6O_4(OH)_4BPDC_{4.52}BPYDC_{0.54}BA_{0.6}FA_{0.09}Pt_{0.25}$, where BA and FA is benzoate and formate, respectively.

Prior to TEM, CO-pulse chemisorption the MOF samples were reduced for 4 hours at 350°C (5 °C/min ramp) in 20 ml/(min·0.1g_{cat}) flow of 10 % H_2/Ar under ambient pressure, then cooled to room temperature in inert flow (20 ml/min Ar).

The turnover frequency (TOF) of a catalyst is defined as the number of reactant molecules converted to products over one active catalyst site per second. The number of exposed (active) Pt surface sites (N_APt) for each catalyst was calculated by two methods; the first method was based on CO pulse chemisorption experiments, assuming a CO_{ads}:Pt ratio of 1:1. The second method was based on the average Pt nanoparticle (NP) size determined from TEM measurements. In this case, all exposed Pt atoms on the NP surface were considered active sites, and it was assumed that all Pt was reduced and present in the form of Pt NPs. Furthermore, it was assumed that the Pt NPs were spherical; in good agreement with the TEM images:

$\boldsymbol{V_{Pt}(NP) = 4/3 \cdot \pi \cdot (d/2)^3}$ (volume of a Pt NP with diameter $\mathbf{d = D}$) (1)

$\mathbf{m_{Pt}(NP)} = \boldsymbol{\rho_{Pt}} \cdot \mathbf{V_{Pt}(NP)}$ (mass of Pt per NP. $\boldsymbol{\rho_{Pt}}$ is the bulk density of Pt metal) (2)

$\mathbf{N_{Pt}(NP) = n_{Pt}(NP) \cdot N_A}$ (nr. of Pt atoms in one NP. $\mathbf{n_{Pt}(NP)}$ is mol Pt in one NP, $\mathbf{N_A}$ is Avogadro's number) (3)

Calculations 1–3 are repeated for a particle with diameter $\mathbf{d} = \mathbf{D\text{-}2 \cdot d_{Pt,atom}}$, where $\mathbf{d_{Pt,atom}}$ is the diameter of a Pt atom.

The number of surface Pt atoms in a Pt NP with diameter $\mathbf{d = D}$ is given by

$$\mathbf{N_{surf,Pt}(NP) = N_{Pt}(NP, d = D) - N_{Pt}(NP, d = D\text{-}2 \cdot d_{Pt,atom})} \qquad (4)$$

The total mol Pt surface atoms per gram catalyst is given by

$\mathbf{N_{surf,Pt} = N_{surf,Pt}(NP)/N_A \cdot m_{Pt}/(Mm_{Pt} \cdot n_{Pt}(NP))}$ ($\mathbf{Mm_{Pt}}$ is Pt molar mass, $\mathbf{m_{Pt}}$ is mass of Pt per g catalyst) (5)

The TOF of each catalyst after a given time on stream (TOS) was calculated using the following formula:

$$\mathbf{TOF\ (s^{-1}) = (}\boldsymbol{C}_{\mathbf{CO2}}\mathbf{/100\%) \cdot Flow_{CO2} \cdot N_A/N_{surf,Pt}} \qquad (6)$$

where C_{CO2} is the CO_2 conversion (in %) and $Flow_{CO2}$ is the CO_2 flow over the catalyst (mol/s).

Table S1. List of m/z values traced for reactants and products during H/D and $^{13}CO_2/^{12}CO_2$ exchange experiments.

Species	**m/z values traced** **H/D**	**$^{13}CO_2/^{12}CO_2$**
Methanol	31, 33, 34, 35, 36	34, 35
Methane	15	21
Water	18, 19	-
CO	28	28,29
Hydrogen	2, 3	4
CO_2	44	44,45

S2. Characterization

N_2 adsorption

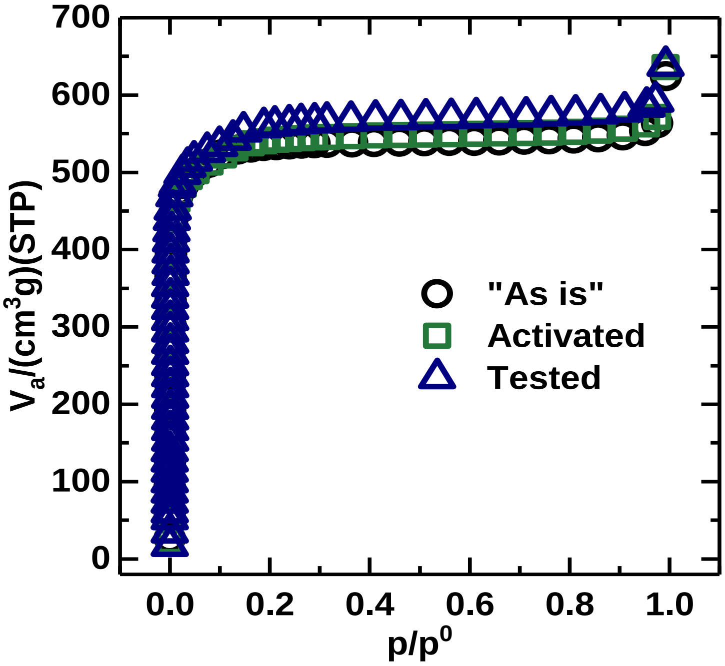

Figure S1. N_2 Adsorption isotherms of UiO-67-Pt after synthesis (black circles), after activation at 350°C in 10% H_2 (green squares) and after testing for CO2 hydrogenation under various conditions for >20 days (mostly at 170°C) (blue triangles). BET specific surface areas are calculated to 2089, 2104 and 2161 m^2/g, for the three samples, respectively.

Powder X-ray Diffraction (pXRD)

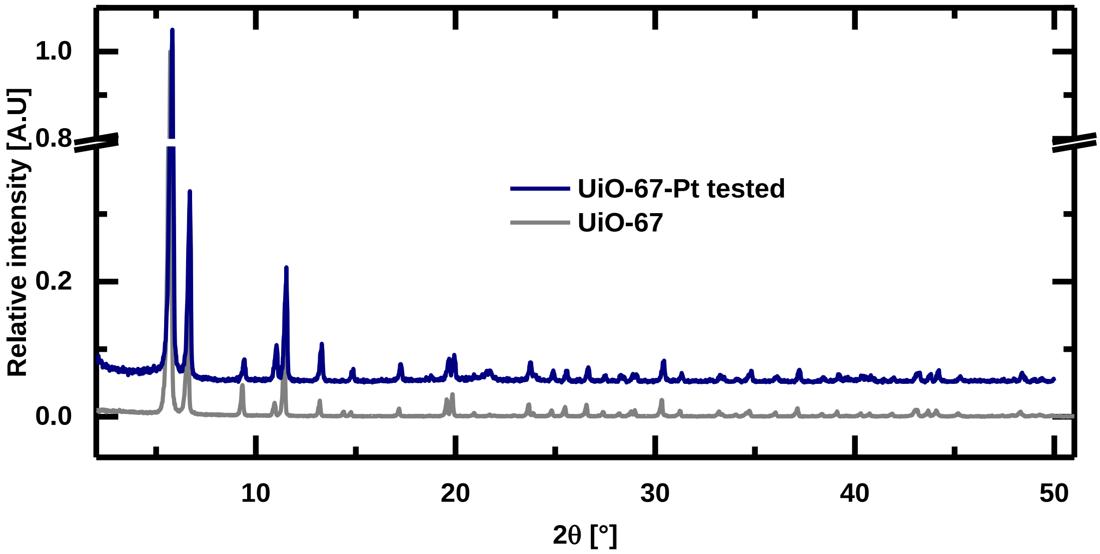

Figure S2. XRD patterns of UiO-67 (grey, bottom) after synthesis and UiO-67-Pt (blue, top) after testing.

Solution state ^{1}H-NMR

Table S2. Solution state ^{1}H-NMR data of UiO-67 (a) and UiO-67-Pt before (b) and after testing(c). The amounts are given as percent with respect to BPDC.

Entry	**Sample**	**BPYDC (w.r.t BPDC)**	**Benzoic acid (w.r.t BPDC)**	**Formic acid (w.r.t BPDC)**
a	UiO-67	11	12.5	2
b	UiO-67 -Pt	9.7	10.8	3.9
c	UiO-67 -Pt after testing	9.6	3.4	0

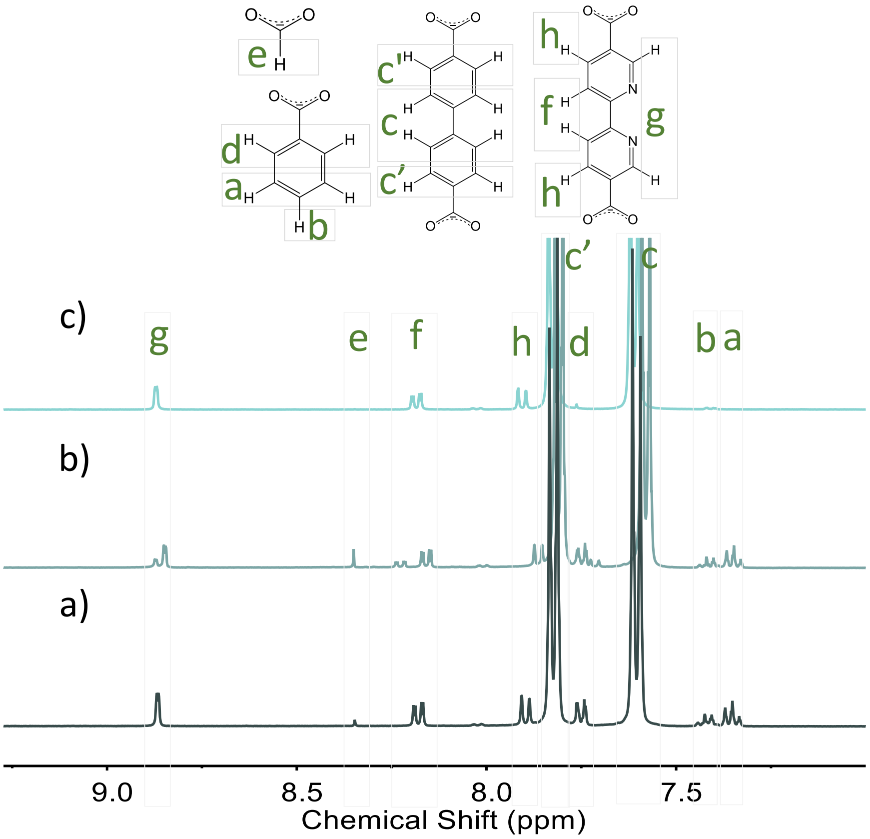

Figure S3. ^{1}H-NMR spectra of a) UiO-67, b) UiO-67-Pt and c) UiO-67-Pt after testing

Thermogravimetric analysis (TGA)

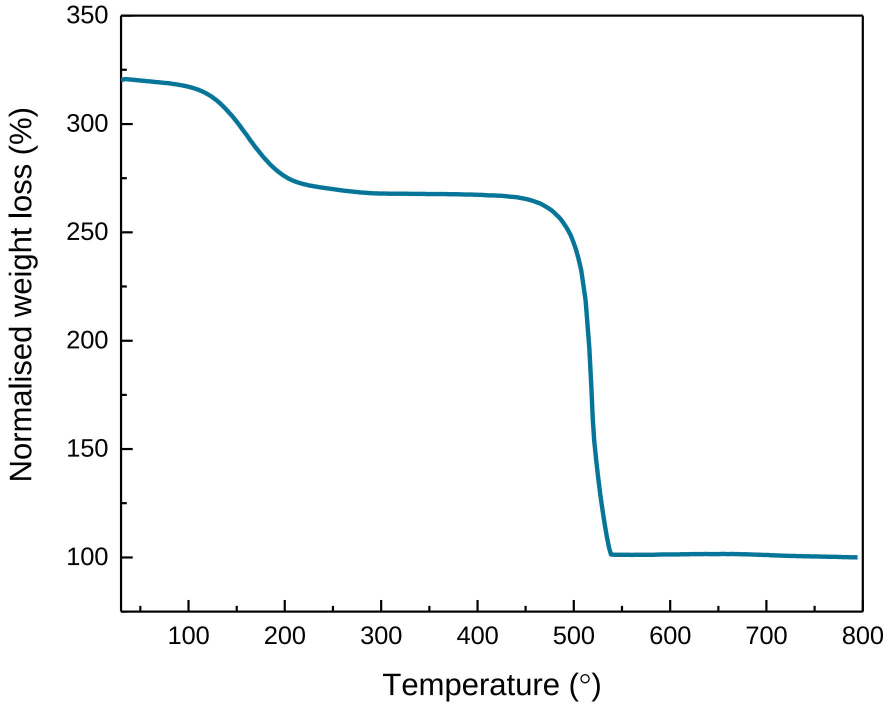

Figure S4. Thermogravimetric analysis of UiO-67 (30 to 800 °C with the ramp rate of 5 °C/min in a mixture of 5 ml/min O_2 and 20 ml/min of N_2).

Table S3. Defectivity of UiO-67-BPYDC estimated from solution state ^{1}H-NMR and TGA. BPDC:Zr cluster (node) = 6 in the perfect UiO-67 system.

MOF	**Wt %$_{400\ °C}$**	**BPDC: node**	**BPYDC: node**	**BA: node**	**FA: Zr node**
UiO-67	267	4.52	0.54	0.60	0.09

Transmission electron microscopy (TEM)

Transmission electron microscopy (TEM) and high resolution TEM (HR-TEM) measurements were performed using a side entry Jeol JEM 3010 (300 kV) microscope equipped with a LaB_6 filament and fitted with X-ray EDS analysis by a Link ISIS 200 detector. For analyses, the powdered samples were deposited on a copper grid, coated with a porous carbon film. All digital micrographs were acquired using an Ultrascan 1000 camera and the images were processed by Gatan digital micrograph. A statistically representative number of particles was counted in order to obtain the Pt particle size distributions. The mean particle diameter (d_m) was calculated as follows: $d_m = \Sigma d_i n_i / \Sigma n_i$, where n_i was the number of particles of diameter d_i. The measurements were carried out on UiO-67-Pt after activation at 4 hours at 350 °C in 20 ml/(min·0.1g_{cat}) 10 % H_2/Ar (Figure S5) and after 6 days of testing at 170 °C and 240 °C (Figure S6). It is worth noting that the UiO-67-Pt samples proved to be stable to prolonged exposition under the electron beam of the instrument, in terms of UiO-67 crystallinity as well as Pt NPs size (no metal coalescence).

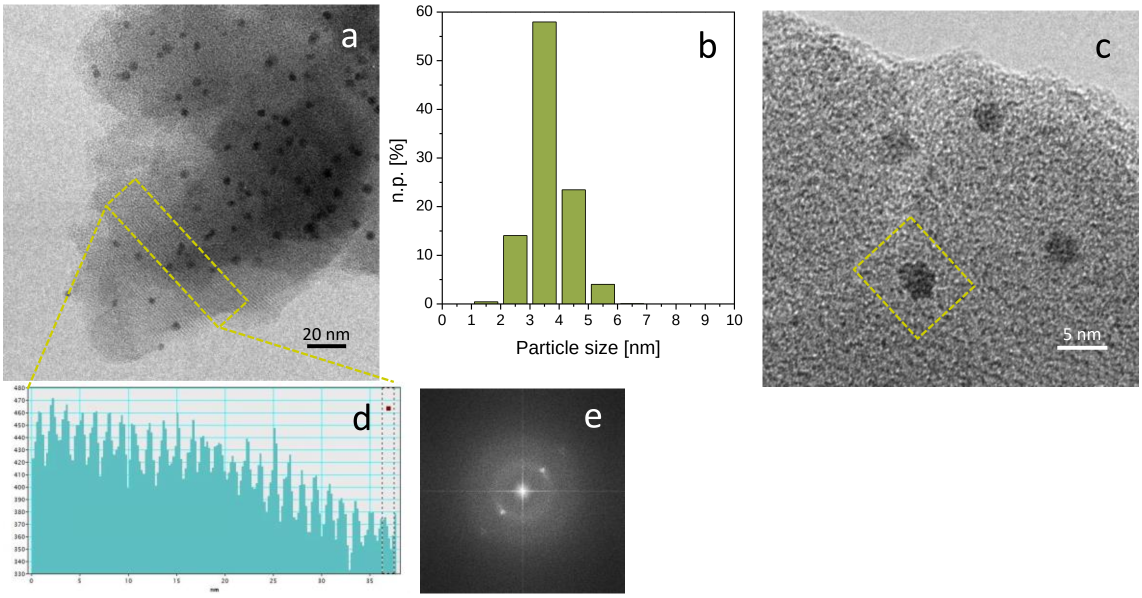

Figure S5. a) HRTEM of UiO-67-Pt after activation for 4 hours at 350°C in 20 ml/(minx0.1g$_{cat}$) 10% H_2/Ar. b) Pt NP size distribution (more than 1000 NPs were counted) (d_m = to 3.6 ± 0.7 nm). c) High magnification HRTEM image of Pt NPs. d) Measure of the spacing between the diffraction fringes observed in the zone highlighted by the green box in a). e) Fourier Transform of the image in a). Instrumental magnification: 100000× and 300000×, respectively.

Pt NPs were observed mainly as large particle agglomerates on 5% Pt/SiO_2, pointing out poor stabilization of the NPs on the SiO_2 support. Despite this feature, the particle size distribution was built and an average size of 5.0 ± 2.0 nm was estimated (Figure S7) (the images have been taken on several different regions of the grid).

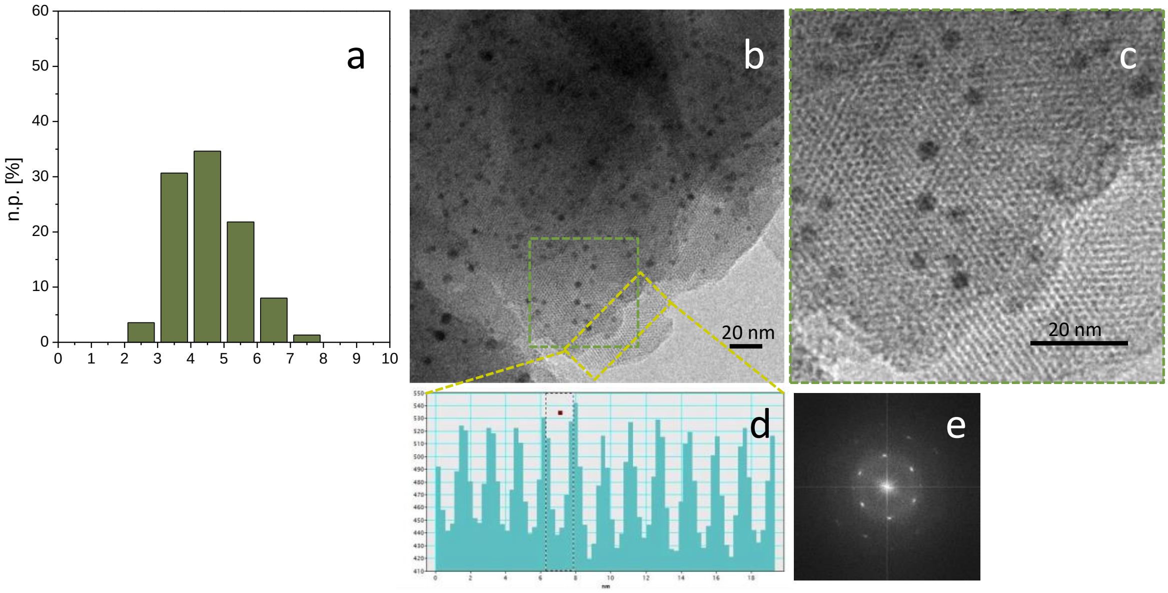

Figure S6. a) Pt NP size distribution of UiO-67-Pt after activation for 4 hours at 350 °C in 20 ml/(min·0.1g_{cat}) 10% H_2/Ar and 6 days of testing at 170 °C and 240 °C (about 1000 NPs were counted) (d_m = to 4.5 ± 1.0 nm). b) HRTEM image of the catalyst. c) Zoom of the region highlighted by a green square in the HRTEM image reported in b) in which the Pt NPs are supported on UiO-67 viewed along the [111] direction. d) Measure of the spacing between the diffraction fringes observed in the zone highlighted by the light green box in b). e) Fourier Transform of the image in b). Instrumental magnification: 80000×.

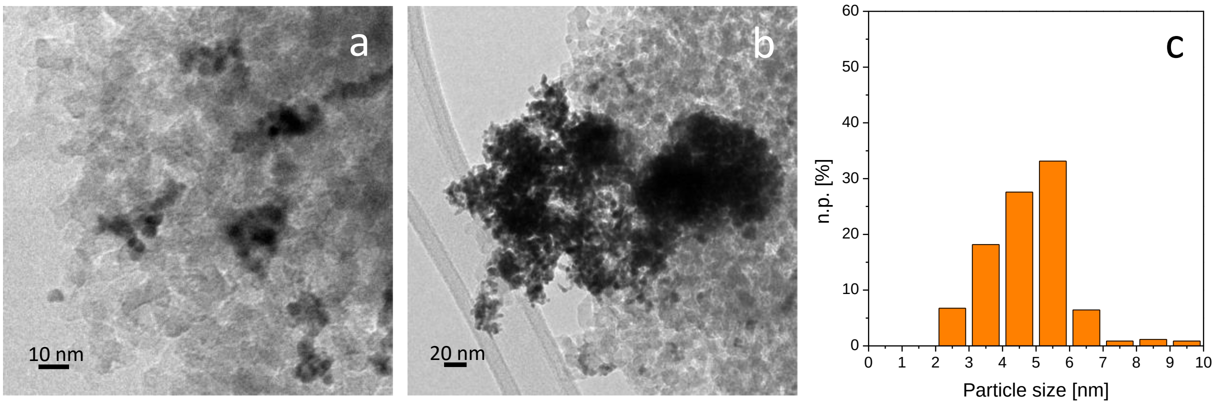

Figure S7. a) TEM image of 5%Pt/SiO_2. b) TEM image of a big agglomerate of Pt NPs. c) Pt NP size distribution (about 400 NPs were counted). Instrumental magnification: 150000× and 50000×, respectively.

Activation of UiO-67-Pt

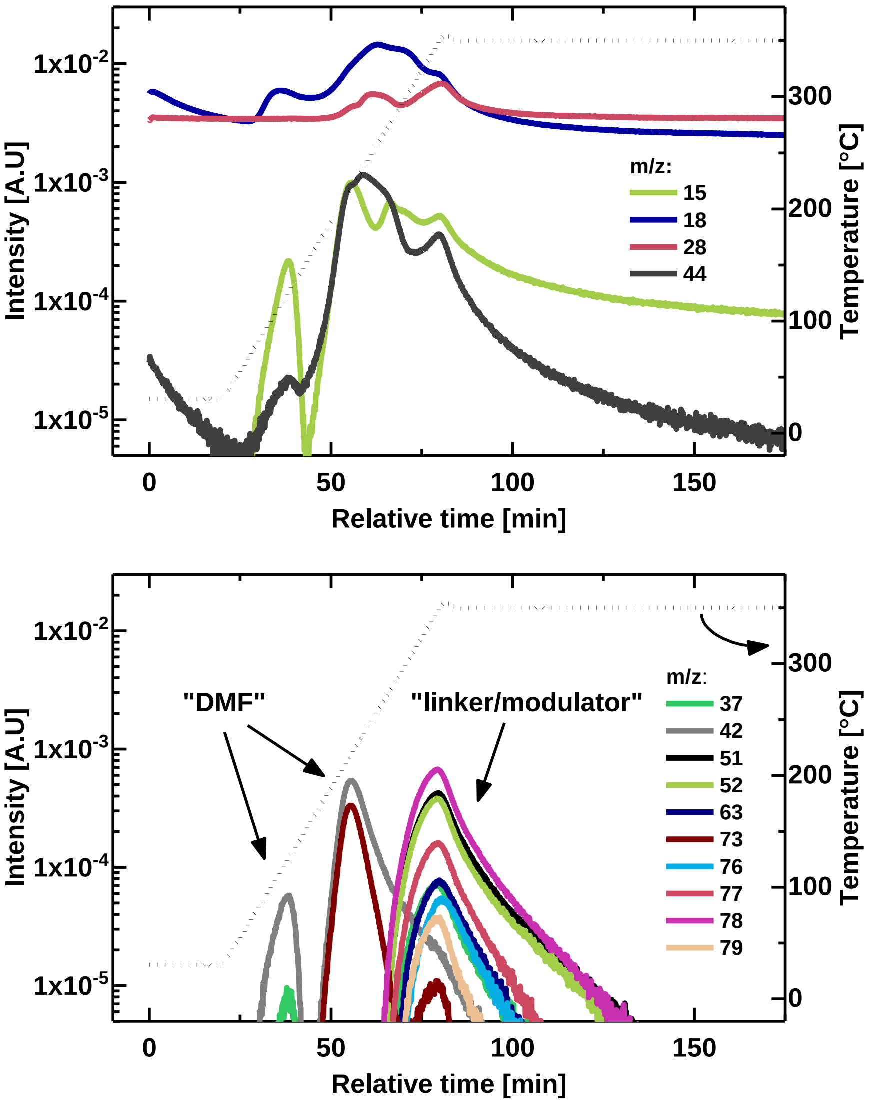

Figure S8. On-line MS signals during activation on UiO-67-Pt. Conditions: 5 °C/min ramp to 350°C (4 h dwell) in 20 ml/(min·0.1g_{cat}) flow of 10 % H_2/Ar. "DMF" indicates the signal-peaks presumably related to DMF and DMF-derived species. "linker/modulator" indicates the signal-peak presumably related to linker and modulator species. During a 2nd activation, no significant signals of "DMF" and "linker/modulator" type were observed.

S3. Catalytic Testing

Methanol turn-over-frequency (TOF) over UiO-67-Pt and Pt/Al_2O_3

UiO-67-Pt: The CH_3OH TOF of 0.01 s^{-1} reported in-text is calculated from the methanol rate of formation (1.62×10^{-8} mol/(s·g_{cat})) and the number of exposed Pt surface atoms determined by CO-chemisorption at RT (1.7 µmol/g_{cat}) (Figure 1 and Table 1). Conditions: τ = 0.01 g_{cat}·min/ml, 8 bar, 170 °C, CO_2/H_2/inert = 1/6/3.

Pt/Al_2O_3: CH_3OH TOF = 0.0001 s^{-1}, rate = 3.55×10^{-9} mol/(s·g_{cat}), **$N_{A,CO,RT}$** = 36 µmol/g_{cat} (Figure 1 and Table 1). Conditions: τ = 0.02 g_{cat}·min/ml, 8 bar, 170 °C, CO_2/H_2/inert = 1/6/3.

H/D exchange during CO_2 hydrogenation over different Pt/support combinations

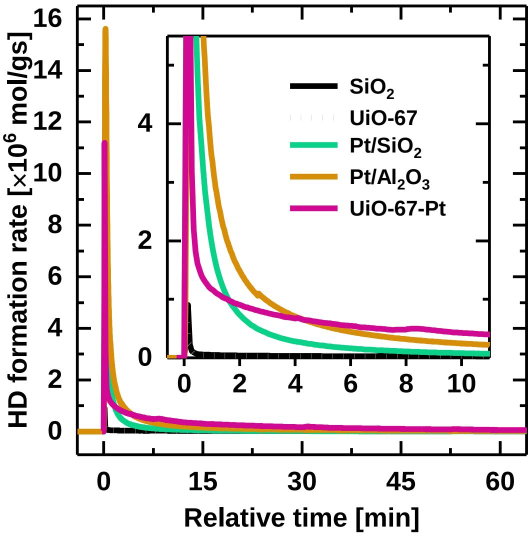

Figure S9. The HD formation rate after switching from H_2+CO_2 to D_2+CO_2 over UiO-67-Pt, Pt/Al_2O_3, Pt/SiO_2, UiO-67 and SiO_2. T = 170 °C and P = 1 bar.

Kinetic investigation: partial pressure and contact time variation

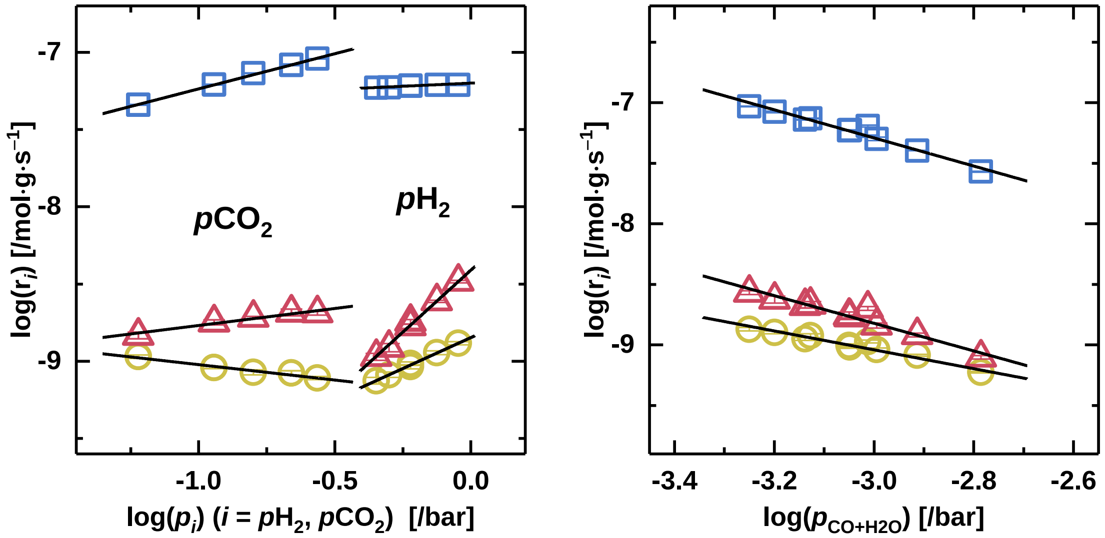

Figure S10. **Left**: pCO_2 (left) and pH_2 (right) partial pressure dependency at 170 °C (1 bar) of CO (squares), CH_4 (circles) and CH_3OH (triangles). pH_2 = 0.6 and pCO_2 = 0.1 when pCO_2 and pH_2 is varied, respectively. **Right:** $CO+H_2O$ partial pressure dependence of CO, CH_4 and CH_3OH formation rates. The CO+ H_2O partial pressure is as half the measured effluent CO and H_2O outlet concentrations during contact time variation (see Figure 5). The experiment is performed at 170 °C, 1 bar, 1/6/3 $CO_2/H_2/He$ and $\tau = 0.004–0.04\ g_{cat}\cdot min/ml$.

Table S4 Reaction orders in pH_2 and pCO_2 , prior to $p(CO+H_2O)$ correction, for the rate of conversion (X) and CO, CH_4 and CH_3OH formation at 170 °C (P_{tot} = 1 bar) over UiO-67-Pt. pCO_2 = 0.1 and pH_2 = 0.6 when varying pH_2 and pCO_2, respectively.

p_i	**X**	**CO**	**CH_4**	**CH_3OH**
H_2	0.1	0.1	0.8	1.6
CO_2	0.5	0.5	-0.2	0.2

The reaction orders in total pressure, pH_2, pCO_2 and $p(CO+H_2O)$ for CO, CH_4 and CH_3OH formation over UiO-67-Pt are listed in Table 2 and Table S4. The influence of total pressure is negligible on the rate of CO formation and minor on the rate CH_4 formation, as evident from the zero and 0.3 order in total pressure, respectively. The reaction order in total pressure is, in contrast, substantially larger (first order) for the rate of methanol formation, suggesting that reactant coverage is a limiting factor in the reaction. In our previous work on UiO-67-Pt,[1] we reported a 0.3 and 0.5 order in pH_2 and pCO_2, respectively, for the rate of CO formation at 240–260 °C. At 170°C, the order in pH_2 is even smaller (0.1), while it is unchanged in pCO_2 (Fig. 2). The marginal order in pH_2 suggests that the availability of hydrogen is not critical in the rate-limiting step (RLS) of the RWGS reaction. For the formation of CH_4 and CH_3OH on the other hand, the partial pressure of H_2 is vital compared to CO. The surprisingly large 1.6 order in pH_2 for CH_3OH formation points toward the accessibility of H_2 as strongly rate limiting. For CH_4 and CH_3OH formation, a negative and positive 0.2 order in pCO_2 is observed for the two products respectively. A negative order in pCO_2 clearly suggests that the inhibition effect by a species formed with increasing pCO_2 is greater than the positive effect of increase pCO_2 alone.[2]

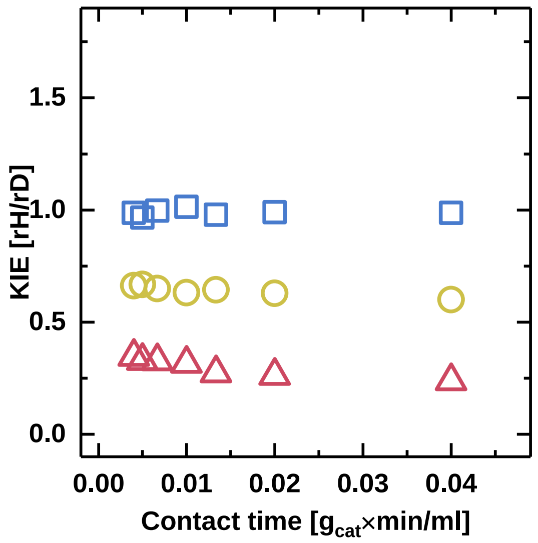

Figure S11. Isotope effect, r_H/r_D, for CO (squares), CH_4 (circles) and CH_3OH (triangles) during CO_2 hydrogenation at 170 °C, 1 bar, 1/6/3 $CO_2/H_2/He$ and $\tau = 0.004 - 0.04$

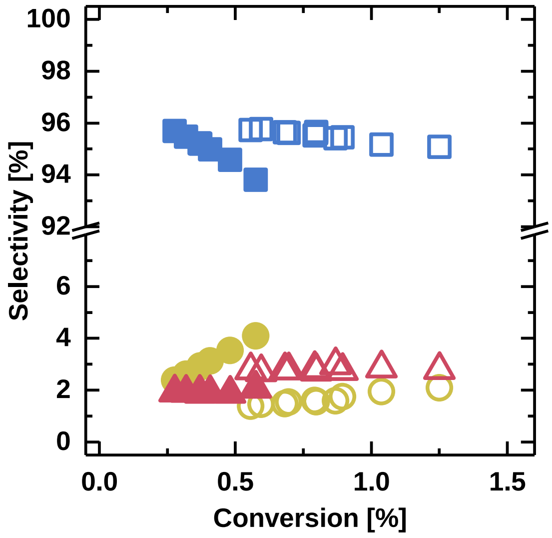

Figure S12. Contact time variation experiment during CO_2 hydrogenation at 170 °C, 1 bar, 1/6/3 $CO_2/H_2/He$ and $\tau = 0.004 - 0.04$ g_{cat}·min/ml. CO (squares), CH_4 (circles) and CH_3OH (triangles) selectivity versus conversion over UiO-67-Pt (open) and Pt/Al_2O_3 (filled).

H/D and $^{13}CO_2/^{12}CO_2$ SSITKA and H/D isotope effects

The transient evolution of 13-labeled CO_2, inert Kr and products when switching from $^{13}CO_2$ + D_2 to $^{12}CO_2$ + D_2 at t = 0 is shown in Figure 3. Both Kr and $^{13}CO_2$ decreased rapidly to zero, suggesting little gas-holdup in the reactor and a weak interaction between the catalyst and CO_2.[3] The normalized intensities of the ^{13}C-labelled products decreased much slower than the inert and CO_2 responses.

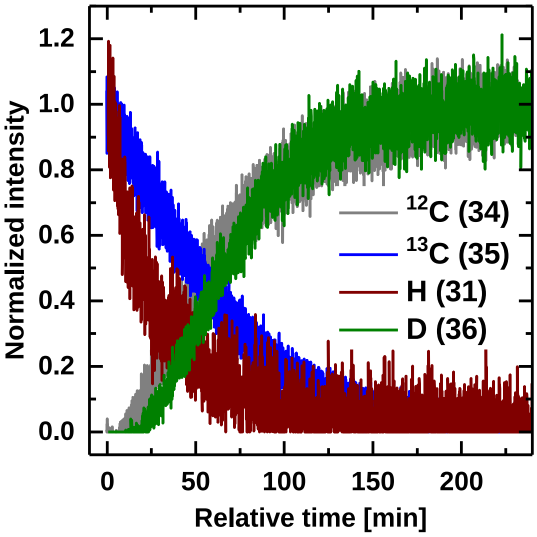

Figure S13. Comparison of methanol during $^{13}CO_2$/$^{12}CO_2$ exchange (m/z = 35/34) and during H/D exchange (m/z = 31/36).

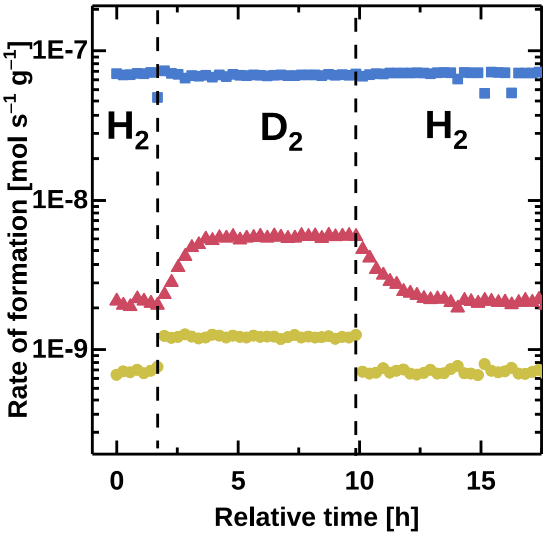

Figure S14. H/D SSITKA during CO_2 hydrogenation at 170 °C, 1bar. Rate of CO (blue squares), methane (yellow circles) and methanol (red triangles) formation over UiO-67-Pt versus time when switching between H_2+CO_2 and D_2+CO_2 in intervals of 8 hours. The rate of methane and methanol is the sum of all isotopologs.

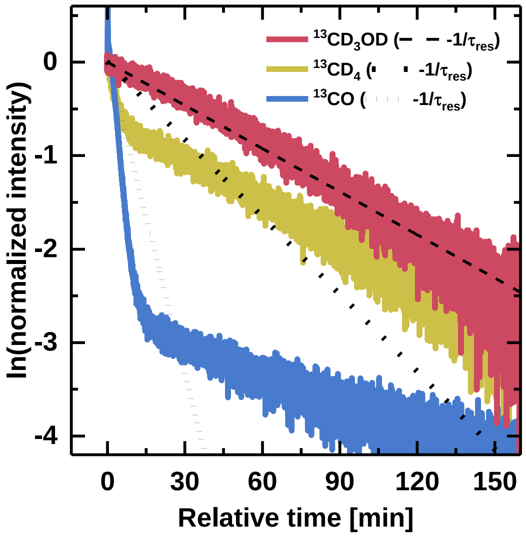

Figure S15. Semi-logarithmic plot of the normalized transient responses of ^{13}CO (m/z = 29), $^{13}CD_4$ (m/z = 21) and $^{13}CD_3OD$ (m/z = 35) products when switching from $^{13}CO_2$ +D_2 to $^{12}CO_2$ +D_2 at t = 0. T = 170 °C, 1bar, τ =0.01 g_{cat}·min/ml. Lines with slopes inversely proportional to the mean surface residence time ($-1/\tau_{res}$) of the respective products are included.

Table S5. Isotope effect (r_H/r_D,) at full isotope equilibration, on the rate of CO, CH_4 and CH_3OH formation at 170 °C (1 bar).

Catalyst	**CO**	**CH4**	**CH3OH**
UiO-67-Pt	1.03	0.58	0.36
Pt/Al$_2$O$_3$	1.07	0.47	0.40
Cu/ZnO/Al$_2$O$_3$ [4]	0.86[a]	-	0.57[a]

[a] 230 °C, 30 bar.

S4. Operando FTIR

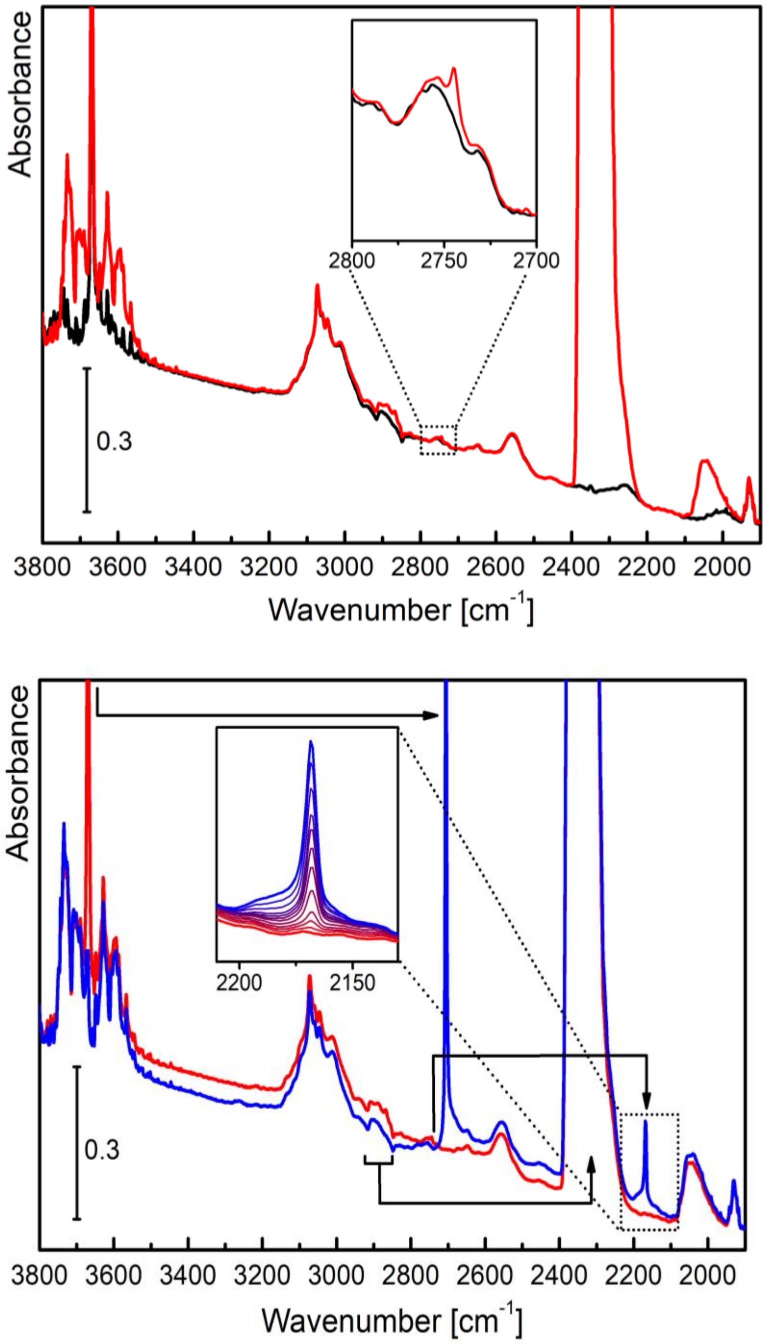

Figure S16. Top: FT-IR spectra of UiO-67-Pt collected during CO_2 hydrogenation (CO_2/H_2 = 1/6, 10 ml/min, 170 °C, 1 bar) at different times (thick black curve for t=0 min, thick red curve for t = 120 min). The inset is a reminder of what is shown in Figure 2 in the main text. Bottom: FT-IR spectra of UiO-67-Pt experiencing the effect of H/D isotopic exchange during CO_2 hydrogenation ($CO_2/H_2(D_2)$=1/6, 10 ml/min, 170 °C, 1 bar). Red line represents the catalyst after 120 min in hydrogenation conditions and the blue represents the catalyst 120 min after the switch to deuteration conditions. The inset shows a magnification of the ν(C-D) stretching of deuterated formates bound to Zr nodes in the UiO-67 framework (time evolution from red to blue curve).

Figure S16 compares the FT-IR spectra of UiO-67-Pt sample right after the activation procedure (black) with the one collected after 120 min in reaction conditions (CO_2:H_2=1:6, 10 ml/min, 170 °C, 1 bar - red curve). The spectra coincide in most of the intervals, hereafter shortly described: i) ν(O-H) stretching region, in which both spectra are characterized by the sharp peak at 3670 cm^{-1} related to the Zr-μ_3OH at the cornerstones.[5, 6] In case of the spectrum collected in CO_2 flux, the roto-vibrational overtones of the gaseous phase are very intense and overshadow the spectrum in that region; ii) ν(C-H_{arom}) stretching, belonging to the biphenyl and bipyridine type linkers are arising in 3200–3000 cm^{-1} interval.[5, 6] Only in case of the sample treated in CO_2/H_2, a very strong signal centred at 2340 cm^{-1} is due to the roto-vibrational profile of gaseous CO_2. Moreover, a broad signal between 2100 and 1950 cm^{-1} can be easily associated to carbon monoxide, linearly chemisorbed on metal nanoparticles (in end-on configuration).[1] Weak bands are observed it the region 2700-3000 cm^{-1} and have been assigned to various combination modes of C-H from formate groups. A more complete view of the vibrational features of formate is reported in the spectrum reported in Figure S17. Among these signals, 2745 cm^{-1} is assigned to the bidentate coordinated formate groups on the cornerstones of the MOF lacking a connection with a linker or with the modulator (benzoic acid).[7-9]

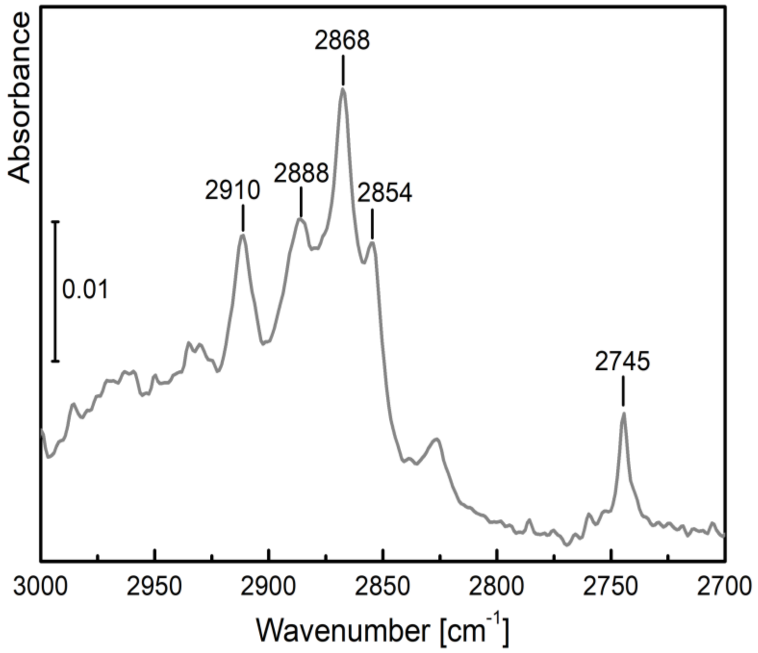

Figure S17. FT-IR spectrum highlighting the formate groups region for UiO-67-Pt. The spectrum represent the sample during CO_2 hydrogenation (CO_2/H_2 = 1/6, 10 ml/min, 170 °C, 1 bar) after the subtraction of the activated sample (10% H_2 at 350 °C for 4 h).

S5. Computational Details

Energy calculations and geometry optimizations

The potential energy of the various structures was computed by periodic DFT calculations. The mixed Gaussian and plane wave method (GPW),[10-12] as implemented in CP2K, version 6.1[13, 14] was used; the functional being PBE+D3[15, 16] with the Gaussian basis set DZVP-MOLOPT-SR-GTH.[17] The core electrons were represented by norm-conserving, separable dual-space GTH-PBE small core pseudopotentials.[18, 19] The Gaussian basis functions were mapped onto a multigrid of size 5. The cutoffs of the five grids were determined by the kinetic energy cut-off of the plane wave basis of 360 Ry and the grid level progression factor of 3. A relative cut-off of 60 Ry determined onto which of the five grids a given Gaussian function should be mapped. The parameter EPS_DEFAULT was set to $1.0 \cdot 10^{-10}$, and the Brillouin zone was sampled at the gamma point.

For systems with band gap, such as the pure UiO-67-BPYDC, the reactant and product molecules, the efficient orbital transformation (OT) method[20] was used. The OT minimizer was the direct inversion in the iterative subspace (DIIS), and the preconditioner was FULL_ALL with an energy gap of 0.001 a.u.

For metallic systems, i.e. UiO-67-BPYDC with Pt nanoparticle, the orbital transformation is inefficient. For these systems, we resorted to computing the energy through a traditional diagonalization algorithm. The lower efficiency of this algorithm was counteracted by the use of the efficient ELPA library.[21] The orbital occupation numbers were “smeared” according to the Fermi-Dirac distribution using an electronic temperature of 100 K. A Broyden mixing was employed with the following parameters: alpha = 0.1, beta = 1.5, nbroyden = 8. The default value of the SCF convergence criteria ($1.0\ 10^{-5}$ a.u.) was used. The chosen Gaussian and plane wave basis set were based on values used in previous works[22] as well as our own convergence test (see Table S6). The convergence test consisted in checking how the relative energies of three isomers of Pt_{55}@UiO-67-BPYDC, primitive unit cell, changed upon increasing the kinetic energy cutoff. We deemed a kinetic energy cutoff of 360 Ry and a relative cutoff of 60 Ry to correspond to a converged potential energy.

Table S6. Convergence test of the kinetic energy cutoff, E^{kin}(cutoff). Values of E^{kin}(cutoff) in the range from 360 to 660 Ry and values of 60 and 80 Ry of the relative cutoff, REL_CUTOFF were tested. Energies, ΔE_{rel}, (in kJ/mol) are relative to **IS1.**

IS2	**REL_CUTOFF** = 60 Ry	**REL_CUTOFF** = 80 Ry
E_{kin}(cutoff) / Ry	ΔE_{rel} / kJ/mol	ΔE_{rel} / kJ/mol
360	-98.00	-98.00
420	-97.37	-97.37
480	-97.53	-97.53
500	-97.53	-97.53

540	-97.69	-97.69
600	-97.64	-97.64
660	-97.66	-97.65
IS3		
E_{kin}(cutoff) / Ry	ΔE_{rel} / kJ/mol	ΔE_{rel} / kJ/mol
360	35.06	35.07
420	35.15	35.15
480	35.86	35.86
500	35.86	35.86
540	35.58	35.58
600	35.55	35.55
660	35.57	35.57

For optimizations of the atomic coordinates, the BFGS optimizer was used. The geometries were considered converged when the maximum and RMS gradients and the maximum and RMS displacements were below $4.5 \cdot 10^{-4}$ and $3.0 \cdot 10^{-4}$ Ha Bohr^{-1} and $3.0 \cdot 10^{-3}$ and $1.5 \cdot 10^{-3}$ Bohr, respectively.

For the combined optimization of atomic coordinates and cell parameters, the kinetic energy cut-off was increased to 720 Ry. The BFGS optimizer was used, and the convergence criteria on the gradients and the displacements were the same as for the geometry optimizations. The external pressure was 1 bar and the pressure tolerance was set to 10 bar.

Computation of free energy

The free energy was computed to assess the stability of the materials as well as the gas phase species. For the materials, we use two approximations to the free energy. For adsorbed intermediates, we included only the vibrational contribution to the free energy. A numerical partial Hessian was computed involving only the atoms of the adsorbates. A central difference method was used and the atoms were displaced 0.015 Å in positive and negative direction along the x, y, and z coordinates.

When computing the reaction free energy of the formation of $\mathbf{Pt_{55}}^{\mathbf{tet}}$ and $\mathbf{Pt_{89}}^{\mathbf{tet}}$, $\Delta G_r(\mathbf{Pt_{55}}^{\mathbf{tet}})$ and $\Delta G_r(\mathbf{Pt_{89}}^{\mathbf{tet}})$, respectively, we included for the materials both the vibrational and configurational contributions. In the computation of the numerical partial Hessian, we included all Pt atoms of the nanoparticle + the linkers defining the tetrahedral cage. For the structures without nanoparticles, the atoms of the linkers defining the tetrahedral cage were included.

The change in the configurational contribution to the reaction free energy, ΔG_{confg}, was computed from the change in the configurational entropy as

$$\Delta G_{\mathrm{config}} = -T \cdot \Delta S_{\mathrm{config}}$$

where T = 623 K is the temperature of the catalyst activation. $\Delta S_{\mathrm{confg}}$ is the change in configurational entropy from the start to the end of the reaction

$$\Delta S_{\mathrm{config}} = S_{\mathrm{config,end}} - S_{\mathrm{config,start}}$$

$$\Delta S_{\mathrm{config}} = kT \ln W$$

where W is the number of microstates. In these systems, we count the number of microstates as the product of the number of ways of distributing the nanoparticle (NP) and the number of ways of distributing the BPYDC linker. There are eight tetrahedral cages per unit cell, and the NP can be distributed in $\binom{8 \cdot N_{\mathrm{cells}}}{N_{\mathrm{NP}}}$ ways, where N_{cells} is the number of unit cells involved in the reaction (see Figure S19). Furthermore, there are 24 linkers per unit cell, and the BPYDC linker can be distributed in $\binom{24 \cdot N_{\mathrm{cells}}}{1 \cdot N_{\mathrm{cells}}}$ ways. The number of microstates is therefore

$$W = \binom{8 \cdot N_{\mathrm{cells}}}{N_{\mathrm{NP}}} \cdot \binom{24 \cdot N_{\mathrm{cells}}}{1 \cdot N_{\mathrm{cells}}}$$

The configurational contribution to the free energy, $\Delta G_{\mathrm{config}}$, is then for $\mathbf{Pt_{55}^{tet}}$ and $\mathbf{Pt_{89}^{tet}}$, $\Delta G_{\mathrm{config,Pt_{55}^{tet}}} = -32$ kJ/mol and $\Delta G_{\mathrm{config,Pt_{89}^{tet}}} = -34$ kJ/mol

For gas phase species, H_2 and CO_2, all atoms were included in the computation of the numerical Hessian. Their rotation and translations also contribute to the free energies were computed analytically based on the partition functions for an ideal gas. For convenience, Gaussian 16[23] was used to compute these contributions. The ideal gas approximation was employed in the computation of the PV term, PV = nRT, where n = 1 and R = 8.31446 J/(K·mol). The temperature of the free energy calculations was set to T = 443 K for the catalytic reactions and to T = 623 K for the catalyst activation.

Selection of the model system

Preliminary computations were carried out to find where in the UiO-67-BPYDC lattice the Pt nanoparticle (NP) preferred to be located. A cuboctahedral Pt_{55} NP was placed in the octahedral, $\mathbf{Pt_{55}^{oct}}$, and tetrahedral cage, $\mathbf{Pt_{55}^{tet}}$, respectively (see Figure S18), and the energy of the optimized structures shows a clear preference for the tetrahedral cage. We rationalize this preference by the larger amount of Pt-linker interactions in that structure; and we can generalize this result by noting that the NP in $\mathbf{Pt_{55}^{tet}}$ fills the tetrahedral cage to a larger degree than the NP in $\mathbf{Pt_{55}^{oct}}$ fills the octahedral cage. Thus, for a NP of a given size, its preferred location will be in a cage it is able to fill to a larger degree and thus maximize the amount of Pt-linker interactions.

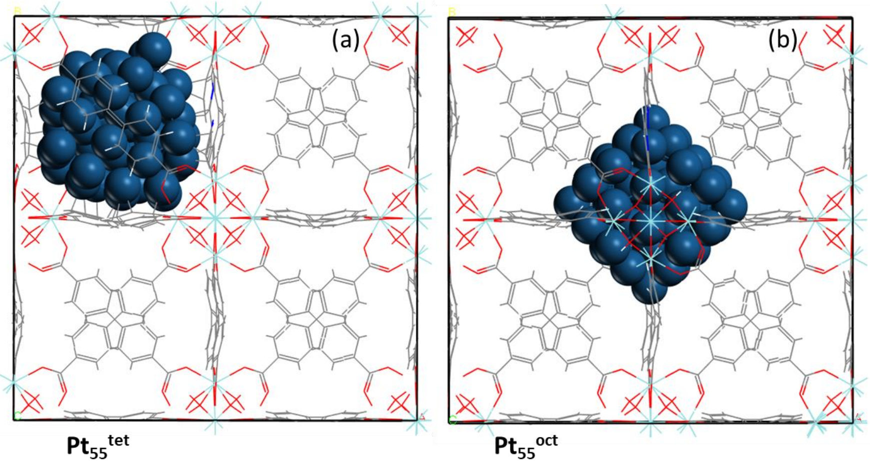

Figure S18. Computed structures of embedded Pt_{55} in UiO-67-BPYDC. (a) Pt_{55} located in the tetrahedral cage, $\mathbf{Pt_{55}^{tet}}$, ΔE = 0 kJ/mol. (b) Pt_{55} located in the octahedral cage, $\mathbf{Pt_{55}^{oct}}$, ΔE = 1111 kJ/mol.

We then explore how favorable the growth would be of the Pt-NP in the tetrahedral cage. To better understand the thermodynamics of the Pt NP growth, the reaction free energy, ΔGr, of forming $\mathbf{Pt_{55}^{tet}}$ $\mathbf{Pt_{63}^{tet}}$, $\mathbf{Pt_{71}^{tet}}$ and $\mathbf{Pt_{89}^{tet}}$ from the starting compound $PtCl_2$ was computed (see Figure S19 for a schematic illustration). The reaction free energy of the four NPs, $\Delta G_r(\mathbf{Pt_{55}^{tet}}) = -68$ kJ/mol, $\Delta G_r(\mathbf{Pt_{63}^{tet}}) = -215$ kJ/mol , $\Delta G_r(\mathbf{Pt_{71}^{tet}}) = -246$ kJ/mol and $\Delta G_r(\mathbf{Pt_{89}^{tet}}) = -989$ kJ/mol ($\mathbf{Pt_{55}^{tet}}$ and $\mathbf{Pt_{89}^{tet}}$ are shown in Figure S20) shows that the energy decrease as the NP grows. Furthermore, a linear regression ($R^2 = 0.95$) shows that this decrease is linear (coefficient = -30 kJ/(mol· N_{Pt}) with respect to the number of Pt atoms added. A plot with the data points and the trend line is shown in Figure S21. The addition of further Pt atoms was not attempted because the linear trend was already apparent from the four data points. Therefore, we proceed with the study on the formate formation from the $\mathbf{Pt_{89}^{tet}}$ system because it was the most stable structure.

In addition, we observed that at this size, the decoordination of one of the oxygen of the linkers became exergonic by 54 kJ/mol, while the complete decoordination is endergonic by 15 kJ/mol (L^1 and L^0, in Figure 4). These results indicate that the displacement of the linker could be overcome by increasing the Pt NP.

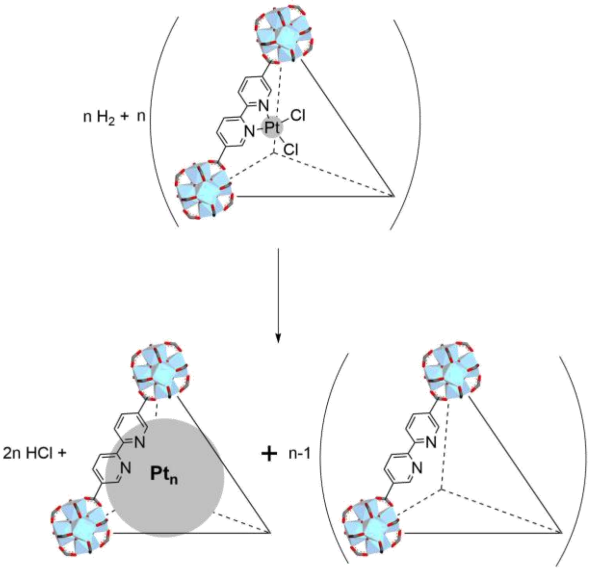

Figure S19. Schematic representation of the formation of Pt NP from $PtCl_2$ linkers under a reducing H_2 atmosphere.

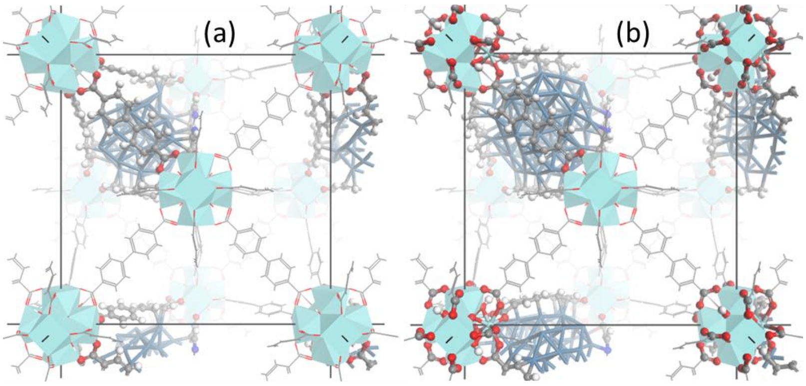

$\mathbf{Pt_{55}}^{tet}$ $\mathbf{Pt_{89}}^{tet}$

Figure S20. Optimized structures of (a) $\mathbf{Pt_{55}}^{tet}$, $\Delta G_r(\mathbf{Pt_{55}}^{tet})$ = -68 kJ/mol and (b) $\mathbf{Pt_{89}}^{tet}$, $\Delta G_r(\mathbf{Pt_{89}}^{tet})$ = -989 kJ/mol.

Handling of small imaginary frequencies

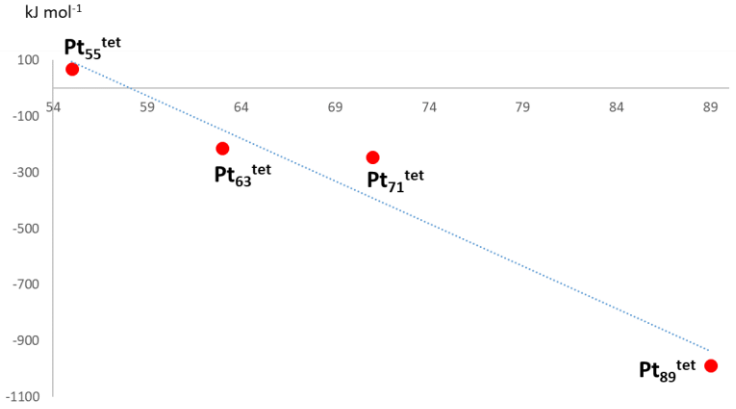

Figure S21. Reaction free energy, ΔG_r, (in kJ/mol) of Pt_n^{tet} for n = 55, 63, 71, 89, as a function of number of Pt atoms, n.

For the BPYDC and BPYDC-$PtCl_2$ structures shown in Figure S21, the initial frequency calculation resulted in small imaginary frequencies. For the BPYDC structure, the initial attempt resulted in an imaginary frequency of 3.2i cm^{-1}. A re-optimization, and a subsequent frequency calculation, with EPS_SCF decreased to $1.0{\cdot}10^{-6}$ a.u. resulted in real frequencies only, with the smallest one being 15.0 cm^{-1}. At 623 K, a frequency of 15.0 cm^{-1} contributes -17 kJ/mol to the free energy. Decreasing EPS_SCF to $1.0 \cdot 10^{-6}$ a.u. increased the total energy by 1 kJ/mol.

For the BPYDC-$PtCl_2$ structure, the initial frequency calculation resulted in three imaginary frequencies, 14.4i, 8.6i, and 3.7i cm^{-1}. A re-optimization, and subsequent frequency calculation, with EPS_SCF decreased to $1.0{\cdot}10^{-6}$ a.u. reduced the number of imaginary frequencies to one, 12.1i cm^{-1}. This imaginary frequency had the same value even after decreasing EPS_SCF to $1.0{\cdot}10^{-9}$ a.u. We therefore deemed EPS_SCF = $1.0{\cdot}10^{-6}$ a.u. to give sufficiently accurate frequencies. Continuing from the frequency calculation computed with EPS_SCF = $1.0{\cdot}10^{-6}$ a.u, the structure was displaced in the negative direction along the eigenmode corresponding to the imaginary frequency and re-optimized with a subsequent frequency calculation. This re-optimization resulted in real frequencies only, the smallest one being 6.5 cm^{-1}. In the reaction free energies of Pt_n^{tet}, the free energy of BPYDC-$PtCl_2$ is multiplied by *n* (See Figure S21). Getting rid of all imaginary frequencies is therefore vital in order to avoid substantial errors in the computation of the reaction free energy.

Preferred CO_2 coordination in Pt_{89}^{tet}

The formation of formate from **L^1** complex (see Figure 4) involves the adsorption of a CO_2 molecule. Three modes of adsorption were checked (see Figure S22): i) coordination of the O atom to the opened Zr-site, L^1-CO*O^1, $\Delta G(\mathbf{Pt}_{\mathbf{89}}^{\mathbf{tet}} + CO_2 \rightarrow L^1\text{-CO*}O^1) = -6$ kJ/mol, ii) coordination of the C atom to the Pt surface, L^1-C*O_2^0, $\Delta G(\mathbf{Pt}_{\mathbf{89}}^{\mathbf{tet}} + CO_2 \rightarrow L^1\text{-C*}O_2^0) = -30$ kJ/mol, and iii) coordination of the C atom to the Pt surface and the O atom to the opened Zr-site, L^1-C*O_2^1, $\Delta G(\mathbf{Pt}_{\mathbf{89}}^{\mathbf{tet}} + CO_2 \rightarrow L^1\text{-C*}O_2^1) = -74$ kJ/mol. Of these only L^1-C*O_2^1 corresponds to an exergonic free energy of adsorption, $\Delta G_{ads}(\mathbf{Pt}_{\mathbf{89}}^{\mathbf{tet}}\mathbf{\text{-}I} + CO_2 \rightarrow L^1\text{-C*}O_2^1) = -20$ kJ/mol. Because L^1-C*O_2^1 corresponds to the most favorable mode of CO_2 adsorption, the formate formation pathway was continued from that structure (see Figure 4).

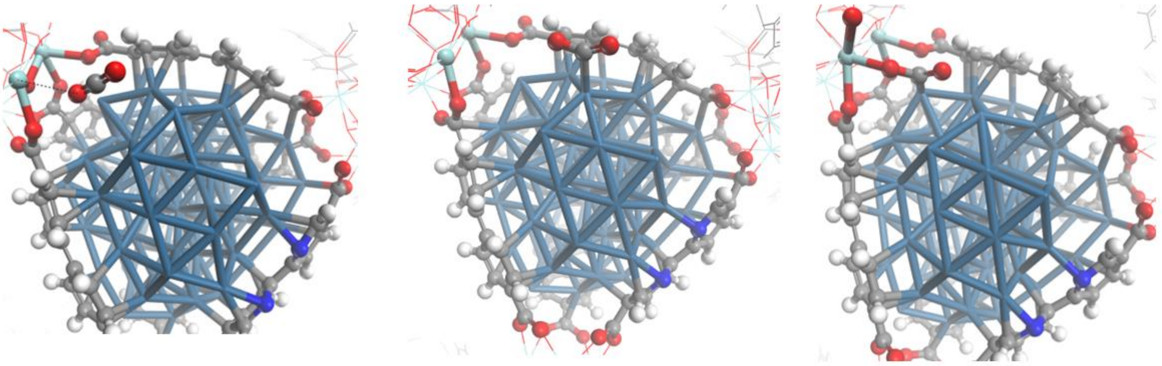

L^1-CO*O^1 **L^1-C*O_2^0** **L^1-C*O_2^1**

Figure S22. Three modes of CO_2 adsorption to $\mathbf{Pt}_{\mathbf{89}}^{\mathbf{tet}}\mathbf{\text{-}I}$. L^1-CO*O^1, $\Delta G(\mathbf{Pt}_{\mathbf{89}}^{\mathbf{tet}} + CO_2 \rightarrow L^1\text{-CO*}O^1) = -6$ kJ/mol, L^1-C*O_2^0, $\Delta G(\mathbf{Pt}_{\mathbf{89}}^{\mathbf{tet}} + CO_2 \rightarrow L^1\text{-C*}O_2^0) = -30$ kJ/mol, L^1-C*O_2^1, $\Delta G(\mathbf{Pt}_{\mathbf{89}}^{\mathbf{tet}} + CO_2 \rightarrow L^1\text{-C*}O_2^1) = -74$ kJ/mol.

Computational experiment

Structure L^0-HCO_2^1+H* resulting from orienting the formate moiety of L^0-HCO_2^2+H* to a Zr-monodentate configuration is shown in Figure S23.

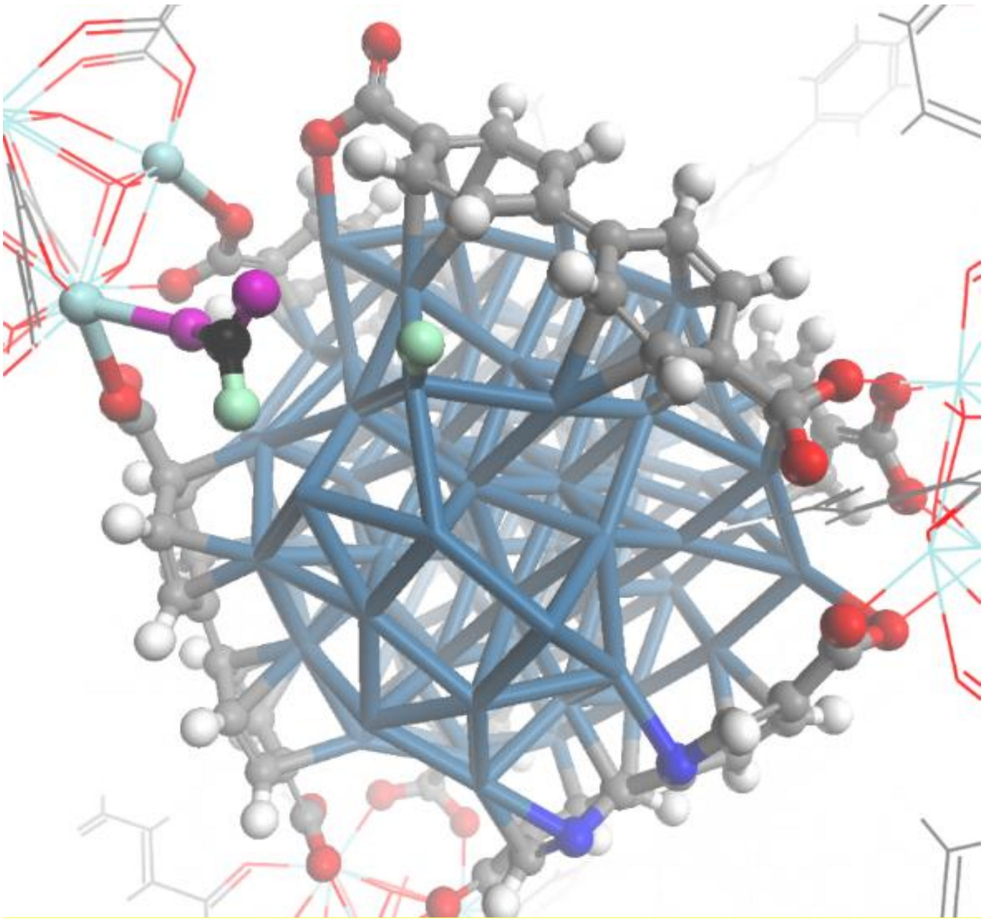

Figure S23. Structure L^0-$HCO_2{}^1$+H* resulting from orienting the formate moiety of L^0-$HCO_2{}^2$+H* to a Zr-monodentate configuration. Color code: H = white, C = grey, O = red, N = blue, Zr = cyan, Pt = dark blue. Color code, reacting species: H = light green, C = black O = purple.

References

1. Gutterød, E. S.; Øien-Ødegaard, S.; Bossers, K.; Nieuwelink, A.-E.; Manzoli, M.; Braglia, L.; Lazzarini, A.; Borfecchia, E.; Ahmadigoltapeh, S.; Bouchevreau, B.; Lønstad-Bleken, B. T.; Henry, R.; Lamberti, C.; Bordiga, S.; Weckhuysen, B. M.; Lillerud, K. P.; Olsbye, U., CO2 Hydrogenation over Pt-Containing UiO-67 Zr-MOFs—The Base Case. *Ind. Eng. Chem. Res.* **2017,** *56* (45), 13206-13218.
2. Wang, X.; Shi, H.; Kwak, J. H.; Szanyi, J., Mechanism of CO2 Hydrogenation on Pd/Al2O3 Catalysts: Kinetics and Transient DRIFTS-MS Studies. *ACS Catal.* **2015,** *5* (11), 6337-6349.
3. Wang, X.; Shi, H.; Szanyi, J., Controlling selectivities in CO2 reduction through mechanistic understanding. *Nat. Commun.* **2017,** *8* (1), 513.
4. Kunkes, E. L.; Studt, F.; Abild-Pedersen, F.; Schlögl, R.; Behrens, M., Hydrogenation of CO2 to methanol and CO on Cu/ZnO/Al2O3: Is there a common intermediate or not? *J. Catal.* **2015,** *328*, 43-48.
5. Chavan, S.; Vitillo, J. G.; Gianolio, D.; Zavorotynska, O.; Civalleri, B.; Jakobsen, S.; Nilsen, M. H.; Valenzano, L.; Lamberti, C.; Lillerud, K. P.; Bordiga, S., H2storage in isostructural UiO-67 and UiO-66 MOFs. *Phys. Chem. Chem. Phys.* **2012,** *14* (5), 1614-1626.
6. Kandiah, M.; Usseglio, S.; Svelle, S.; Olsbye, U.; Lillerud, K. P.; Tilset, M., Post-synthetic modification of the metal–organic framework compound UiO-66. *J. Mater. Chem.* **2010,** *20* (44), 9848-9851.
7. Yang, D.; Ortuño, M. A.; Bernales, V.; Cramer, C. J.; Gagliardi, L.; Gates, B. C., Structure and Dynamics of Zr6O8 Metal–Organic Framework Node Surfaces Probed with Ethanol Dehydration as a Catalytic Test Reaction. *J. Am. Chem. Soc.* **2018,** *140* (10), 3751-3759.

8. Tibiletti, D.; Meunier, F. C.; Goguet, A.; Reid, D.; Burch, R.; Boaro, M.; Vicario, M.; Trovarelli, A., An investigation of possible mechanisms for the water–gas shift reaction over a ZrO2-supported Pt catalyst. *J. Catal.* **2006,** *244* (2), 183-191.

9. Busca, G.; Lamotte, J.; Lavalley, J. C.; Lorenzelli, V., FT-IR study of the adsorption and transformation of formaldehyde on oxide surfaces. *J. Am. Chem. Soc.* **1987,** *109* (17), 5197-5202.

10. Lippert, G.; Hutter, J.; Parrinello, M., The Gaussian and augmented-plane-wave density functional method for ab initio molecular dynamics simulations. *Theor. Chem. Acc.* **1999,** *103*, 124-140.

11. Lippert, G.; Hutter, J.; Parrinello, M., A hybrid Gaussian and plane wave density functional scheme. *Mol. Phys.* **1997,** *92* (3), 477-487.

12. VandeVondele, J.; Krack, M.; Mohamed, F., Quickstep: Fast and accurate density functional calculations using a mixed Gaussian and plane waves approach. *Comput. Phys. Commun.* **2005,** *167*, 103-128.

13. Group, C. K. D. *CP2K*, version 6.1; 2018.

14. Hutter, J.; Iannuzzi, M.; Schiffmann, F.; VandeVondele, J., CP2K: atomistic simulations of condensed matter systems. *WIREs Comput. Mol. Sci.* **2014,** *4*, 15-25.

15. Grimme, S.; Antony, J.; Ehrlich, S.; Krieg, H., A consistent and accurate ab initio parametrization of density functional dispersion correction (DFT-D) for the 94 elements H-Pu. *J. Chem. Phys.* **2010,** *132*, 154104.

16. Grimme, S.; Ehrlich, S.; Goerigk, L., Effect of the damping function in dispersion corrected density functional theory. *J. Comput. Chem.* **2011,** *32*, 1456-1465.

17. VandeVondele, J.; Hutter, J., Gaussian basis sets for accurate calculations on molecular systems in gas and condensed phases. **2007,** *127* (11), 114105.

18. Hartwigsen, C.; Goedecker, S.; Hutter, J., Relativistic separable dual-space Gaussian pseudopotentials from H to Rn. *Phys. Rev. B* **1998,** *58* (7), 3641-3662.

19. Goedecker, S.; Teter, M.; Hutter, J., Separable dual-space Gaussian pseudopotentials. *Phys. Rev. B* **1996,** *54*, 1703-1710.

20. VandeVondele, J.; Hutter, J., An efficient orbital transformation method for electronic structure calculations. *J. Chem. Phys.* **2003,** *118* (10), 4365-4369.

21. Marek, A.; Blum, V.; Johanni, R.; Havu, V.; Lang, B.; Auckenthaler, T.; Heinecke, A.; Bungartz, H. J.; Lederer, H., The ELPA library: scalable parallel eigenvalue solutions for electronic structure theory and computational science. *J. Phys.: Condens. Matter* **2014,** *26* (21), 213201.

22. Ye, J.; Johnson, K. J., Design of Lewis Pair-Functionalized Metal Organic Frameworks for CO2 Hydrogenation. *ACS Catal.* **2015,** *5*, 2921-2928.

23. Frisch, M. J.; Trucks, G. W.; Schlegel, H. B.; Scuseria, G. E.; Robb, M. A.; Cheeseman, J. R.; Scalmani, G.; Barone, V.; Petersson, G. A.; Nakatsuji, H.; Li, X.; Caricato, M.; Marenich, A. V.; Bloino, J.; Janesko, B. G.; Gomperts, R.; Mennucci, B.; Hratchian, H. P.; Ortiz, J. V.; Izmaylov, A. F.; Sonnenberg, J. L.; Williams; Ding, F.; Lipparini, F.; Egidi, F.; Goings, J.; Peng, B.; Petrone, A.; Henderson, T.; Ranasinghe, D.; Zakrzewski, V. G.; Gao, J.; Rega, N.; Zheng, G.; Liang, W.; Hada, M.; Ehara, M.; Toyota, K.; Fukuda, R.; Hasegawa, J.; Ishida, M.; Nakajima, T.; Honda, Y.; Kitao, O.; Nakai, H.; Vreven, T.; Throssell, K.; Montgomery Jr., J. A.; Peralta, J. E.; Ogliaro, F.; Bearpark, M. J.; Heyd, J. J.; Brothers, E. N.; Kudin, K. N.; Staroverov, V. N.; Keith, T. A.; Kobayashi, R.; Normand, J.; Raghavachari, K.; Rendell, A. P.; Burant, J. C.; Iyengar, S. S.; Tomasi, J.; Cossi, M.; Millam, J. M.; Klene, M.; Adamo, C.; Cammi, R.; Ochterski, J. W.; Martin, R. L.; Morokuma, K.; Farkas, O.; Foresman, J. B.; Fox, D. J. *Gaussian 16 Rev. C.01*, Wallingford, CT, 2016.